AGU PUBLICATIONS

JGR

Journal of Geophysical Research: Atmospheres

RESEARCH ARTICLE
10.1002/2015JD024507

**Key Points:**
- The HTE and its governing mechanisms evolve throughout the winter
- Nonlinear wave interactions and multiple mechanisms are at work
- QBO modulates different wave types at distinct stages of the winter

**Correspondence to:**
I. P. White,
iwhit@bas.ac.uk

**Citation:**
White, I. P., H. Lu, and N. J. Mitchell (2016), Seasonal evolution of the QBO-induced wave forcing and circulation anomalies in the northern winter stratosphere, *J. Geophys. Res. Atmos.*, *121*, 10,411–10,431, doi:10.1002/2015JD024507.

Received 14 NOV 2015
Accepted 25 AUG 2016
Accepted article online 28 AUG 2016
Published online 17 SEP 2016



# Seasonal evolution of the QBO-induced wave forcing and circulation anomalies in the northern winter stratosphere

**Ian P. White[1,2], Hua Lu[1], and Nicholas J. Mitchell[2]**

[1]British Antarctic Survey, Cambridge, UK, [2]Department of Electronic and Electrical Engineering, University of Bath, Bath, UK

**Abstract** Diagnostics of wave-mean-flow and wave-wave interactions in isentropic coordinates are analyzed regarding the mechanisms that govern the Holton-Tan effect (HTE), whereby the tropical quasi-biennial oscillation (QBO) modulates the northern winter stratospheric polar vortex. We find a clear seasonal evolution of a QBO modulation of Rossby waves and linear and nonlinear wave interactions, along with multiple mechanisms at work. In early winter, when the lower stratospheric QBO is easterly, there is enhanced upward stationary planetary-wave activity in the subtropical to midlatitude lower stratosphere. These upward-propagating waves are first refracted toward the zero-wind line. Approximately 1 month later, poleward-propagating wave anomalies appear at midlatitudes as a result of nonlinear wave interactions. The enhanced upward wave propagation appears to be due to a combination of the QBO influence on the latitudinal location of the zero-wind line and the increased midlatitude baroclinicity associated with the QBO-induced meridional circulation. This is further aided by a gradual poleward shift over the winter of the middle-stratospheric waveguide, refracting waves poleward. The associated wave breaking weakens the polar vortex and drives a stronger meridional circulation throughout the lower to middle stratosphere, contributing to the high-latitude warming. It is additionally found that in late winter, the modified high-latitude waveguide associated with the weaker polar vortex, consequently reduces upward-propagating transient planetary waves at high latitudes while simultaneously enhancing upward-propagating synoptic waves at midlatitudes. This highlights the need to view the HTE and its mechanisms as an evolving phenomenon throughout the winter.

## 1. Introduction

During Northern Hemisphere (NH) winter, the strength of the stratospheric polar vortex is affected by the quasi-biennial oscillation (QBO), the equatorial zonal winds that alternate between easterlies and westerlies in the tropical stratosphere [*Holton and Tan*, 1980]. In particular, the polar vortex becomes more disturbed when the lower stratospheric QBO is in its easterly phase (QBOe) and more stable when the QBO is in its westerly phase (QBOw). This phenomenon, first discovered by *Holton and Tan* [1980] and often coined the Holton-Tan effect (HTE hereafter), has been subject to intensive study over the last three decades [*O'Sullivan and Young*, 1992; *O'Sullivan and Dunkerton*, 1994; *Baldwin et al.*, 2001; *Gray et al.*, 2001, 2004; *Ruzmaikin et al.*, 2005; *Naito and Yoden*, 2006; *Pascoe et al.*, 2006; *Lu et al.*, 2008, 2014; *Calvo et al.*, 2009; *Hitchman and Huesmann*, 2009; *Anstey et al.*, 2010; *Naoe and Shibata*, 2010; *Yamashita et al.*, 2011; *Garfinkel et al.*, 2012; *Watson and Gray*, 2014; *White et al.*, 2015]. Despite the fact that the HTE has been robustly observed and successfully reproduced by model simulations, the mechanism(s) that cause the HTE are still a topic of research [*Anstey et al.*, 2010].

The mechanisms that have been proposed, so far, all suggest that a QBO modulation of planetary waves is the key to explaining the HTE. Our current understanding of the QBO modulation of planetary waves can be split into two broad categories: one involves a change in the stratospheric waveguide due to the QBO modulation of the latitudinal location of the zero-wind line (i.e., the critical line for stationary waves) in the subtropics and another involves a change in planetary-wave propagation/breaking due to the QBO-induced meridional circulation's effect on the refractive index. The former was first proposed by *Holton and Tan* [1980] and elaborates as follows. Under QBOe, the zero-wind line in the lower stratosphere is located in the winter hemisphere and acts to narrow the extratropical waveguide in the same hemisphere. This results in upward-propagating quasi-stationary planetary waves from the troposphere to be confined to high latitudes, leading to a more disturbed and weaker polar vortex. Planetary waves can also be reflected from the zero-

wind line back toward the polar vortex meridionally and thus further weaken it [*Tung*, 1979]. Conversely, under QBOw, the zero-wind line is located in the summer hemisphere. This results in a latitudinally wider waveguide in the winter hemisphere that encourages wave propagation away from the polar vortex and thus leads to a less disturbed polar vortex. This mechanism is referred to as the HT mechanism hereafter.

*Gray et al.* [2001, 2004] used mechanistic model simulations to study the changes in the extratropical circulation in relation to tropical wind anomalies. They found that the polar vortex is most sensitive to wind anomalies imposed in the subtropical upper stratosphere with easterly wind anomalies leading to an earlier onset of stratospheric sudden warmings. They argue that planetary waves have deep vertical structures and so are susceptible to the effects of circulation changes throughout the stratosphere. However, it remains inconclusive to distinguish whether the polar-vortex sensitivity was due to the QBO influence on the location of the zero-wind line or the QBO-induced meridional circulation in the upper stratosphere.

The QBO-induced meridional circulation and its role in linking the QBO and the polar vortex has been studied using climate models [e.g., *Garfinkel et al*., 2012] as well as reanalysis data sets [e.g., *Ruzmaikin et al*., 2005; *Lu et al*., 2014]. The QBO induces such a meridional circulation due to the formation of tropical vertically alternating downwelling and upwelling regions that are necessary for maintaining the thermal anomalies associated with the vertical shear zones of the QBO [*Plumb and Bell,* 1982]. It has been suggested that under QBOe, the QBO-induced meridional circulation has an effect on wave propagation via modulating the refractive index, resulting in an increased wave convergence at high latitudes and a weaker polar vortex [*Garfinkel et al*., 2012; *Lu et al*., 2014].

More recently, *White et al.* [2015] found that under QBOe, there is significantly enhanced wave breaking throughout the lower stratosphere that is accompanied by strengthened baroclinic westerly anomalies that arch down from the subtropical middle stratosphere. These subtropical-to-midlatitude wind anomalies are formed to maintain thermal-wind balance between the tropics and the temperature cells in the subtropics to midlatitudes created by the QBO-induced meridional circulation. The corresponding wave and zonal-wind anomalies are shown to be linked to a poleward shift of the subtropical jet in the upper troposphere, which may act to shift the waveguide poleward. The enhanced upward wave propagation from the troposphere to the stratosphere at midlatitudes and the consequent wave breaking would also lead to a stronger meridional circulation and hence a weaker polar vortex. Note that this mechanism differs from the HT mechanism because it links the poleward shift of the stratospheric waveguide to a poleward shift of the subtropical jet in the upper troposphere-lower stratosphere.

One major drawback of the aforementioned mechanistic studies is that the analyses were often aggregated into seasonal averages. This makes it difficult to distinguish between the possibly different mechanisms that are responsible for the HTE if each mechanism only plays a role at a certain stage of the winter. For instance, upward wave propagation can change in late winter as a consequence of the extratropical wind and waveguide anomalies associated with the early winter HTE. Also, if the HT mechanism does play a major role throughout the winter, it is expected that there is an overall reduced wave activity under QBOw and increased wave activity under QBOe at middle to high latitudes. However, previous studies have often found results that disagree with this argument depending on the chosen periods for time averaging. For instance, *Holton and Tan* [1982] found enhanced wave-1 geopotential-height amplitudes in early winter under QBOe but enhanced wave-2 geopotential-height amplitudes in late winter under QBOw. Their findings were later confirmed by *Hu and Tung* [2002] and *Ruzmaikin et al.* [2005], with the former suggesting that the enhancement of wave-2 in late winter may be due to tropospheric changes rather than a direct QBO effect. Similarly, model simulations by *Naito and Yoden* [2006] and *Naoe and Shibata* [2010] also found that the QBO-induced changes in waves 1 and 2, which altered during early and late winter, were not dynamically consistent with the HT mechanism. In particular, *Naoe and Shibata* [2010] found that although there appears to be overall more planetary wave activity under QBOe than QBOw, there is enhanced upward wave-2 at middle to high latitudes under QBOw in early winter and similarly for wave-1 in late winter. More recently, *Lu et al.* [2014] and *White et al.* [2015] found overall enhanced wave activity at high latitudes under QBOw compared to QBOe in the December-to-February average. Such results cannot be fully explained just by using time averages. We argue that the mechanisms which govern the HTE can be better understood through examination of the seasonal evolution of wave-mean-flow interactions.

Because potential vorticity (PV) is conserved on isentropic levels under adiabatic, frictionless conditions, PV and the associated wave-activity diagnostics in isentropic coordinates are most suitable for studying stratospheric wave-mean-flow interactions [*Hoskins et al*., 1985] and thus the HTE and its mechanisms. Many studies have utilized isentropic coordinates and PV tools to study large-scale dynamics both in the troposphere and stratosphere [e.g., *Birner et al*., 2013; *Butler et al*., 2011; *Hitchman and Huesmann*, 2009; *Kunz et al*., 2009; *Martius et al*., 2007], although relatively few have used it to study the HTE. Most recently, *White et al.* [2015] used these tools to examine the mechanisms of the HTE in NH winter based on the December-to-February average, finding evidence of a QBO modulation of Rossby-wave propagation and breaking. During Rossby-wave breaking events, the amplitude of the wave becomes sufficiently large so that the PV contours overturn, resulting in irreversible mixing and a nonlinear cascade of potential enstrophy along isentropic surfaces [e.g., *McIntyre and Palmer,* 1983]. Such a process can be assessed using the potential enstrophy budget [*Smith*, 1983]. Because the HTE involves changes in waveguides and wave breaking, the budget is best represented in isentropic coordinates, rather than in pressure coordinates, where a quasi-geostrophic assumption must be made. It is in this vein that we here utilize these PV-based tools in isentropic coordinates to investigate the seasonal evolution of the HTE and its associated changes of waveguides and wave activity.

This paper studies the seasonal evolution of the QBO-induced NH extratropical circulation changes. Particular focus is to: (1) identify the mechanisms that govern the early winter onset of the HTE; (2) determine the role of linear and nonlinear processes near the lower stratospheric zero-wind line and their relationship with the "fountain-like" feature in the Eliassen-Palm (EP) fluxes found by *White et al.* [2015]; and (3) elucidate on the links between the late winter wave activity changes and the early winter onset of the HTE. This is accomplished by analyzing the associated linear and nonlinear changes in wave activity using wave-mean-flow interaction and wave-wave interaction diagnostics including the PV gradient, the zonal-mean zonal momentum budget, and the potential enstrophy budget in isentropic coordinates. In addition, the QBO modulation of different wave types and their seasonal progression is evaluated, which is relevant as previous studies have shown that the QBO modulates both transient planetary waves and stationary planetary waves differently [e.g., *Lu et al*., 2012].

## 2. Data and Methods

### 2.1. Data

The 6-hourly, 0.7° horizontal resolution, ERA-Interim reanalysis data set from the European Centre for Medium-Range Weather Forecasts (ECMWF) [*Dee et al*., 2011] is utilized. It covers 1979–2014 (36 years in total) and 15 isentropic levels (265, 275, 285, 300, 315, 330, 350, 370, 395, 430, 475, 530, 600, 700, and 850 K) covering ~815 hPa to 10 hPa. The five variables used for this analysis are Ertel's potential vorticity (PV) $P$, the horizontal wind field $u$ and $v$, temperature $T$ and geopotential height $Z$. While PV on the 15 isentropic levels was directly obtained from the ECMWF (http://www.ecmwf.int), the interpolation procedure used to obtain isentropic $u$, $v$, $T$, and $Z$ at 350 K to 850 K from pressure level data is described in *White et al.* [2015]. This data is further extended in this study to the 265–330 K isentropic levels using a linear interpolation scheme.

### 2.2. Diagnostics Tools

#### 2.2.1. Zonal Mean Momentum Budget

Our main diagnostics build largely on the zonal-mean momentum budget, which in spherical isentropic coordinates takes the form

$$\frac{\partial \overline{u}}{\partial t} = -\hat{v}\left(\frac{1}{a\cos\varphi}\left(\overline{u}\cos\varphi\right)_{\varphi} - f\right) - \hat{Q}\,\overline{u}_{\theta} + \overline{\sigma v' P'} + D_1 \tag{1}$$

where $u, v$ are the zonal and meridional velocity components, $\varphi$ the meridional coordinate, $\theta$ the potential temperature, $t$ the time, $P$ the Rossby-Ertel potential vorticity (PV), $f$ the Coriolis parameter, $Q$ the diabatic heating rate, $a$ the Earth's radius, $D_1$ represents gravity-wave effects and other nonconservative terms (including zonal-mean and perturbation friction and diabatic heating terms) [e.g., *Andrews et al*., 1987], and $\sigma = -g^{-1}\partial p/\partial\theta$ is the isentropic density, with $p$ the pressure and $g$ the gravity acceleration. Overbars represent zonal means and primes the deviations therefrom. Hats represent density-weighted zonal averages (i.e., $\hat{B} \equiv \overline{\sigma B}/\overline{\sigma}$ for any field $B$). Subscripts denote derivatives with respect to the subscripted variable. The

physical interpretation of equation (1) can be found in *Andrews* [1987] and was further discussed in *White et al.* [2015] in relation to the HTE. We refer the reader to those papers for more information. The first term on the right-hand side of equation (1) accounts for the meridional advection of zonal-mean absolute vorticity, which is denoted as

$$\Theta = -\hat{v}\left(\left(\bar{u}\cos\varphi\right)_{\varphi}/a\cos\varphi - f\right) \tag{2}$$

hereafter. We here calculate $\Theta$ directly from the daily variables.

The density-weighted eddy PV fluxes $\bar{\sigma}\overline{v'P'}$ on the right-hand side of equation (1) represents the resolved-wave forcing of the mean flow $\bar{u}$. Equatorward PV fluxes ($\bar{\sigma}\overline{v'P'} < 0$) act to weaken the mean flow and drive a poleward circulation ($\Theta > 0$), whereas poleward PV fluxes ($\bar{\sigma}\overline{v'P'} > 0$) act to strengthen the mean flow and drive an equatorward circulation ($\Theta < 0$) [e.g., *Newman et al.*, 2001]. The eddy PV fluxes can also be written as $\bar{\sigma}\overline{v'P'} \approx \nabla\cdot\mathbf{F}/a\bar{\sigma}\cos\varphi$ [e.g., *Andrews,* 1987], where $\nabla\cdot\mathbf{F}$ is the Eliassen-Palm (EP) flux divergence, with $\mathbf{F} = (F^{(\varphi)}, F^{(\theta)})$ the EP flux, which has meridional component $F^{(\varphi)} = -a\bar{\sigma}\,\overline{v'u'}\cos\varphi$ representing the eddy momentum flux and vertical component $F^{(\theta)} = g^{-1}\overline{p'\Psi'_{\lambda}}$ representing the eddy form drag, where $\Psi \equiv c_p T + \Phi$ is the Montgomery stream function with $c_p$ the specific heat capacity at constant pressure, $T$ the temperature, and $\Phi$ the geopotential. The EP flux $\mathbf{F}$ indicates the direction of wave propagation [e.g., *Edmon et al.*, 1980]. To take full advantage of the conservation property of PV on isentropic surfaces, we quantify the wave forcing in the momentum budget using $\bar{\sigma}\overline{v'P'}$. Nevertheless, we have found quantitatively similar results based on the EP flux divergence term $\nabla\cdot\mathbf{F}/a\bar{\sigma}\cos\varphi$ (not shown).

In order to elucidate on the propagation of different types of waves, the EP flux $\mathbf{F}$ is further separated into contributions from planetary and synoptic waves, where planetary waves are here defined as waves with zonal wave numbers 1 and 2 and synoptic waves as those with zonal wave numbers 3–10. Sensitivity to such a definition will be discussed separately at the places where relevant results are presented. However, calculation of $\mathbf{F}$ on a daily time step, prior to averaging over the required time period, mixes the stationary and transient wave contributions, and we hence utilize the following approach to further separate $\mathbf{F}$ into its stationary and transient planetary waves (described, for example, by *Madden and Labitzke* [1981]). To calculate the stationary planetary waves, the variables $u, v, p, \Psi_{\lambda}$ in calculating $\mathbf{F}$ are first averaged over an extended time period (e.g., a month) at each grid point. For a given latitude, they are then filtered longitudinally for zonal wave numbers 1 and 2 before the zonal departures (representing the wave disturbances), and subsequently, $\mathbf{F}$ are calculated. The transient planetary-wave contribution to $\mathbf{F}$ is subsequently calculated as the difference between the $\mathbf{F}$ calculated on a daily time step and the stationary contribution.

The seasonal evolution of the aforementioned wave-mean-flow-interaction diagnostics are calculated using a time-running mean. More specifically, a centered, 31 day running mean is applied to the extended boreal winter period of 1 September to 1 April, with a forward time step of 1 day, and the results are presented in either latitude-time or height-time plots in section 3.

#### 2.2.2. Potential Enstrophy Budget

Potential enstrophy (hereafter enstrophy), given by $\overline{P'^2}/2$, is used here as a measure of the Rossby-wave amplitude. In isentropic coordinates, changes in wave amplitude with time can be described by the enstrophy budget, which can be expressed as

$$\frac{\partial}{\partial t}\left(\frac{\overline{P'^2}}{2}\right) = \underbrace{-\frac{\overline{v'P'}}{a}\frac{\partial\bar{P}}{\partial\varphi}}_{\Gamma_{\mathrm{WMI}}} \underbrace{-\frac{1}{a\cos\varphi}\overline{u'\frac{\partial}{\partial\lambda}\left(\frac{P'^2}{2}\right)}}_{\Gamma_{\mathrm{ZEEF}}} \underbrace{-\frac{1}{a}\overline{v'\frac{\partial}{\partial\varphi}\left(\frac{P'^2}{2}\right)}}_{\Gamma_{\mathrm{MEEF}}} + D_2. \tag{3}$$

It states that the enstrophy tendency (i.e., wave growth/decay) depends on a combination of a few terms which act as sources or sinks of enstrophy [*Smith*, 1985].

The first term on the right-hand side (denoted by $\Gamma_{\mathrm{WMI}}$) represents up/downgradient eddy PV fluxes [*Birner et al.*, 2013]. Downgradient eddy PV fluxes ($\Gamma_{\mathrm{WMI}} > 0$) induce positive enstrophy tendencies, i.e., wave growth ($\partial\left(\overline{P'^2}/2\right)/\partial t > 0$), whereas upgradient eddy PV fluxes ($\Gamma_{\mathrm{WMI}} < 0$) induce negative enstrophy tendencies, i.e., wave decay ($\partial\left(\overline{P'^2}/2\right)/\partial t < 0$). The second and third terms on the right-hand side labeled $\Gamma_{\mathrm{ZEEF}}$ and $\Gamma_{\mathrm{MEEF}}$ represent eddy fluxes of enstrophy in the zonal and meridional directions, respectively. They are triple

correlations between perturbation variables and hence represent the contribution of nonlinear wave-wave interactions to the enstrophy balance [*Birner et al*., 2013]. Positive $\Gamma_{MEEF}$ and/or $\Gamma_{ZEEF}$ (i.e., convergence of enstrophy) induces wave growth, whereas negative $\Gamma_{MEEF}$ and/or $\Gamma_{ZEEF}$ (i.e., divergence of enstrophy) induces wave decay. $D_2$ indicates dissipatory effects as well as the advection of enstrophy by the meridional flow. Because the later effect is 1 order of magnitude smaller than other terms in the domain under consideration (not shown), it is included in $D_2$. The dissipatory processes include diabatic heating and friction, which result in cross-isentropic motion and/or an irreversible mixing of PV and enstrophy [*Haynes and McIntyre,* 1987].

#### 2.2.3. Latitude-Phase-Speed Cospectrum

A zonal-wave number-phase-speed analysis is conducted to examine the QBO modulation of the upward propagation of transient wave activity across the tropopause. The analysis is performed for the vertical component of the EP flux $F^{(\theta)} = g^{-1}\overline{p'\Psi'_\lambda}$ and the method follows that described in *Randel and Held* [1991]. More specifically, daily time series of $p$ and $\Psi_\lambda$ over an extended period (e.g., the 120 day December to March (DJFM) period) are tapered using a Hanning window. A fast Fourier transform (FFT) is then applied to transform the longitude time series into zonal-wave number-frequency space. The cospectral density is calculated, and then the frequency is smoothed using a Gaussian filter, before being interpolated into zonal-wave number-phase-speed space using a phase-speed grid of 1 m $s^{-1}$. The cospectrum is subsequently summed over zonal wave numbers 1–10, whereby a wave number upper bound of 10 is chosen due to our sensitivity tests, which show that waves with zonal wave numbers greater than 10 contribute negligibly to the cospectrum. The cospectra are further separated into zonal wave numbers 1 and 2, 3 and 4, and 5–10 to assess the contributions of transient planetary waves and synoptic waves. We note here that it is only for the latitude-phase-speed cospectral analysis in section 3 (i.e., Figure 10) that an FFT is applied to **F** in both longitude and time. In all other analysis, to split the contributions to **F** into planetary and synoptic waves, the FFT is only applied in longitude (see section 2.2.1).

### 2.3. QBO Definition

The QBO phases are defined in the same way as that in *Hitchman and Huesmann* [2009] and *White et al.* [2015]. Briefly, the QBO is defined here as the vertical difference between the 50 hPa and 70 hPa pressure surfaces (i.e., approximately the 530 K and 475 K isentropic surfaces, respectively) of the deseasonalized zonal-wind anomalies averaged between 5°S and 5°N with $\geq 2$ m $s^{-1}$ indicating QBOw and $\leq -2$ m $s^{-1}$ indicating QBOe. The deseasonalization is performed by subtracting the climatology for the relevant time period. Composite differences between QBOe and QBOw (QBOe—QBOw hereafter) are calculated and the confidence levels determined at the 90% and 95% levels using a two-sided Student's *t* test. To analyze the temporal evolution, the climatology and composite difference are calculated using a 31 day running mean for both the QBO and the corresponding variables, and the analysis is performed for the extended boreal winter period (1 September to 1 April). To account for possible contamination brought about by volcanic aerosols, the 2 years following each of the two major volcanic eruptions (i.e., El Chichón, March 1982 and Mount Pinatubo, June 1991) are excluded from our composite analysis. We nevertheless found that the results are not sensitive to the volcano-affected years. Also, we note that quantitatively similar results can be obtained if the more traditionally used QBO definition at 50 hPa is utilized (i.e., defining the QBO by the direction of the deseasonalized zonal winds at 50 hPa; not shown).

## 3. Results

The seasonal evolution of the QBO modulation of the zonal-mean zonal wind, the wave forcing of the mean flow, and the meridional advection of absolute vorticity are first examined based on the zonal-mean zonal momentum budget (equations (1) and (2)). Corresponding changes in the waveguide and wave propagation are then identified, and the wave activity is further separated into synoptic, and stationary and transient planetary-wave contributions. The linear and nonlinear wave interactions are also examined using the potential enstrophy budget (equation (3)).

Figures 1a and 1b show the climatology (contours) and the QBO composite differences (QBOe-QBOw; shading) of the seasonal evolution of the zonal-mean zonal wind $\bar{u}$ at two isentropic levels; (a) 850 K and (b) 350 K, for the extended boreal winter (September to April). At 850 K, the most prominent climatological feature is the polar vortex, the strong westerly winds which peak in midwinter (i.e., December–January) at ~60°N. At

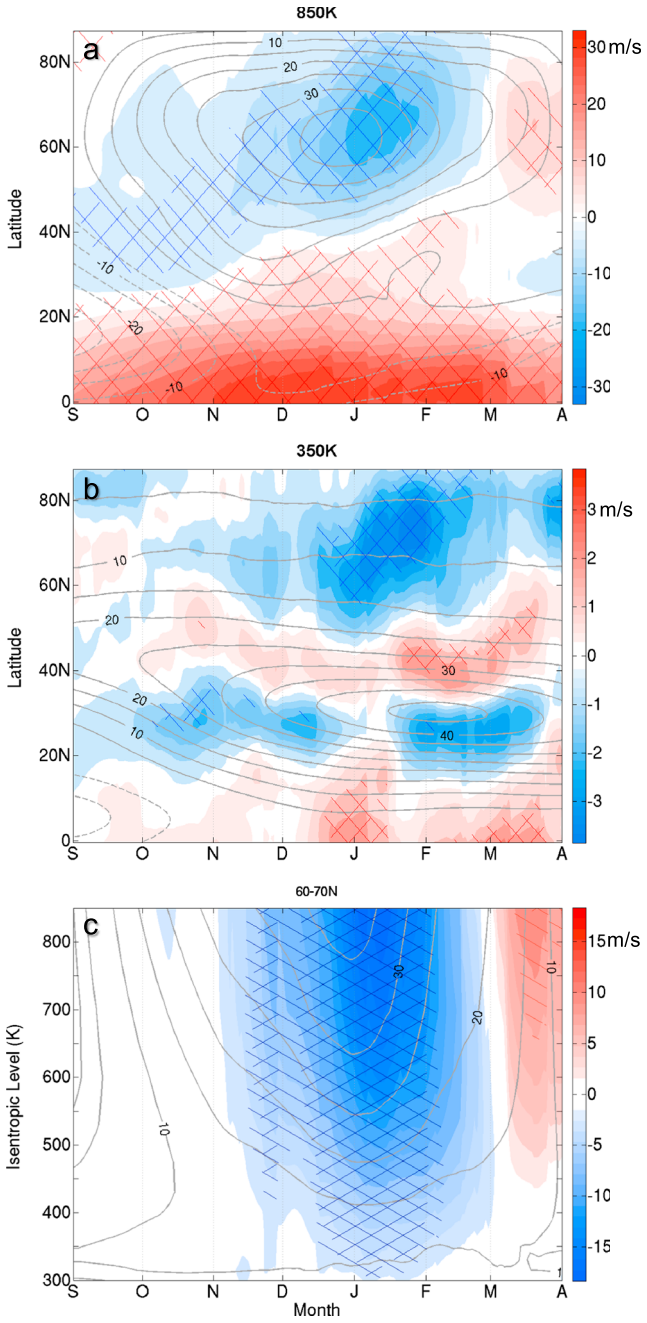


**Figure 1.** (a and b) Seasonal progression of the climatology (contours) and QBO composite difference (QBOe-QBOw; shading) of $\bar{u}$ at 850 K (Figure 1a) and 350 K (Figure 1b) in a time-latitude cross section (September–April, 0–90°N). The analyses are performed on a daily time interval with both the QBO and winds averaged over a 31 day centered window. Unless it is otherwise stated, the same applies for subsequent figures where seasonal progression of a diagnostic variable is shown. Contour interval in the climatology is 5 m $s^{-1}$ with solid and dashed contours representing westerly and easterly winds. Red and blue shading for the composite differences represent positive (i.e., westerly) and negative (i.e., easterly) anomalies. Backward and forward hatchings indicate statistical significance at the 90% and 95% levels. (c): Same as Figure 1a except for the time-height cross section of $\bar{u}$ averaged over the latitude band of 60–70°N.

350 K, the most prominent climatological feature is the subtropical jet that is centered at ~30°N and forms in October–November before reaching its full strength in December–March.

The QBO composite difference highlights a clear HTE at both levels, manifesting itself as negative (i.e., easterly) anomalies northward of ~55°N under QBOe. In particular, at 850 K, the easterly anomalies appear to migrate poleward from near 30°N to high latitudes over winter, with anomalous values inside the polar vortex having magnitudes that are ~40–50% of the climatology during December–January. The large positive (i.e., westerly) anomalies in the tropics represent the QBO westerlies themselves at this level when it is QBOe in the lower stratosphere. The westerly anomalies at high latitudes from late February onward represent the recovery of the polar vortex following the weakening of the vortex in the earlier months.

At 350 K, the QBO-induced zonal-wind anomalies are marked by a dipole pattern with westerly anomalies on the poleward flank of the subtropical jet and easterly anomalies on the equatorward flank throughout the winter period. Despite the fact that only the easterly anomalies in early winter and the westerly anomalies in late winter are statistically significant, this dipole is indicative of a poleward shift of the climatological location of the subtropical jet under QBOe relative to QBOw, which was also previously found by *Garfinkel and Hartmann* [2011] using a climate model. Such a shift is associated with the downward-arching zonal winds of the QBO from near 850 K [see *White et al.*, 2015].

Figure 1c elucidates the vertical extent of the HTE by presenting the seasonal progression of the climatology (contours) and QBO anomalies (shading) of $\bar{u}$ averaged over 60–70°N, displayed in a time-height cross section. The climatological high-latitude winds are westerly throughout boreal winter, increasing in strength with height from 300 K to

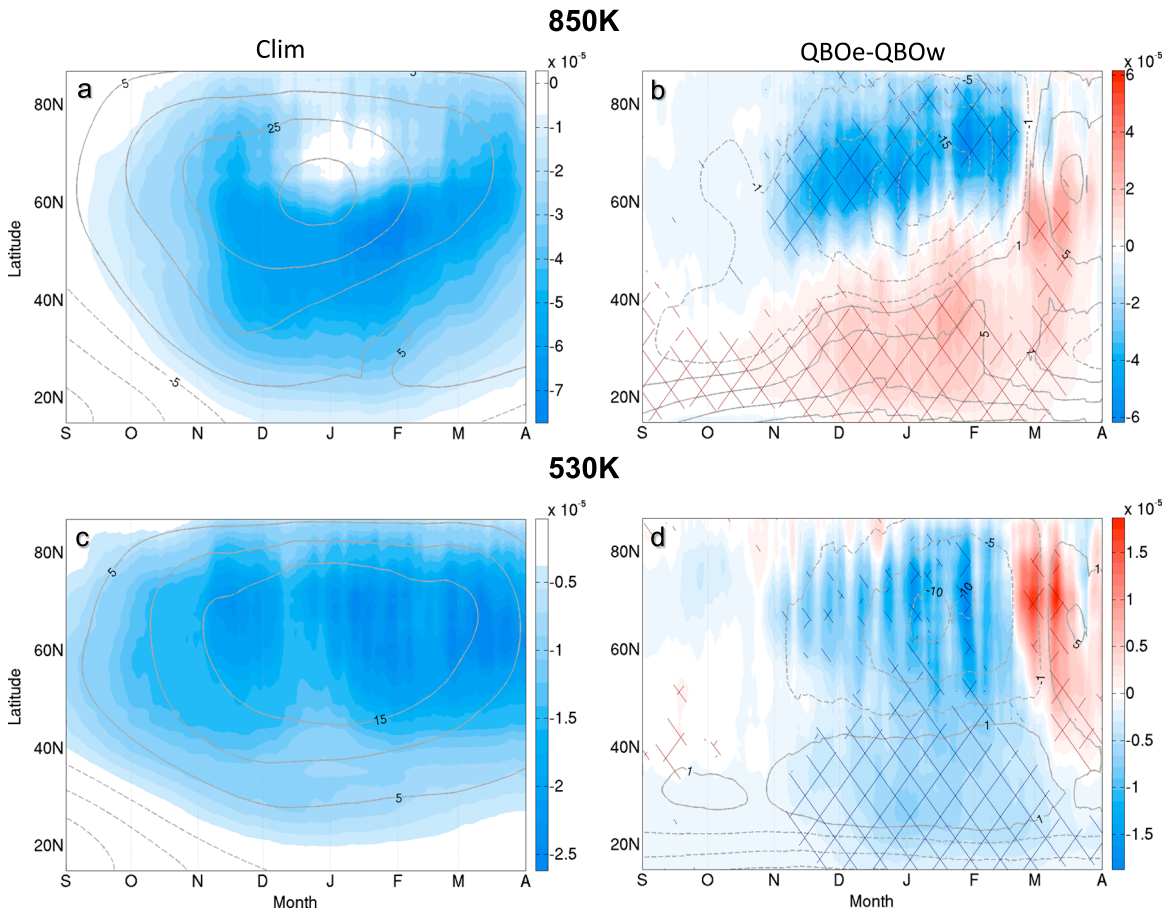


**Figure 2.** (a and b) Seasonal progression of the climatology and QBO composite difference of the density-weighted eddy fluxes of PV $\overline{\sigma v' P'}$ at 850 K. Contours in Figure 2a indicate the climatological winds with intervals at ±5, 15, 25,… m s$^{-1}$, and those in Figure 2b are the QBO-induced anomalous winds with contours at ±1, 5, 10, 15,… m s$^{-1}$. Units of the color bars in m s$^{-2}$. Hatching as in Figure 1. (c and d): Same as Figures 2a and 2b except at 530 K and with the climatological $\bar{u}$ contours having an interval of 5 m s$^{-1}$. Note that the latitude range in this, and all subsequent latitude-time plots, is 15–90°N.

850 K and reaching a maximum of 35 m s$^{-1}$ in December–January. The QBO signal is marked by the easterly anomalies in November–February which represent a weaker polar vortex under QBOe in association with the HTE. These anomalies become more easterly with height (up to −15 m s$^{-1}$ at 850 K) and extend throughout the lower/middle stratosphere in November, before propagating downward from the middle stratosphere (850 K) to the upper troposphere (300 K) during December–January. From late February onward, the westerly anomalies represent a recovery of the polar vortex after the anomalous weakening in earlier months under QBOe. Hereafter, the climatological $\bar{u}$ and its QBO-induced anomalies are superimposed on the plots of other diagnostics to aid in their discussion.

To understand the dynamical cause of these $\bar{u}$ anomalies, the QBO modulation of the wave forcing of the mean flow, measured by the density-weighted eddy fluxes of PV $\overline{\sigma v' P'}$ (see equation (1)), is presented in Figure 2. It shows the seasonal evolution of the climatology and the QBO composite difference at 850 K (Figures 2a and 2b) and at 530 K (Figures 2c and 2d). Note that in the composite difference at 530 K (Figure 2d), the negative $\bar{u}$ anomalies shown in contours represent the easterly winds of the QBO at this level. Note that all seasonal-evolution plots herein are shown from 15°N to 90°N rather than from 0° to 90°N as in Figures 1a and 1b, to facilitate our focus on understanding the extratropical effect of the QBO. The climatologies of $\overline{\sigma v' P'}$ at both levels are characterized by predominately equatorward PV fluxes (equivalently EP flux convergence), acting to advect high PV from high latitudes to low latitudes and hence weakening the polar vortex over the winter. At 850 K, the fluxes are found predominantly on the outer flank of the polar vortex, while at 530 K, they occur over the entire polar vortex. The weak-valued region of $\overline{\sigma v' P'} < 0$ at 850 K near 70°N in midwinter suggests a lack of Rossby-wave penetration into the strong polar vortex during this period.

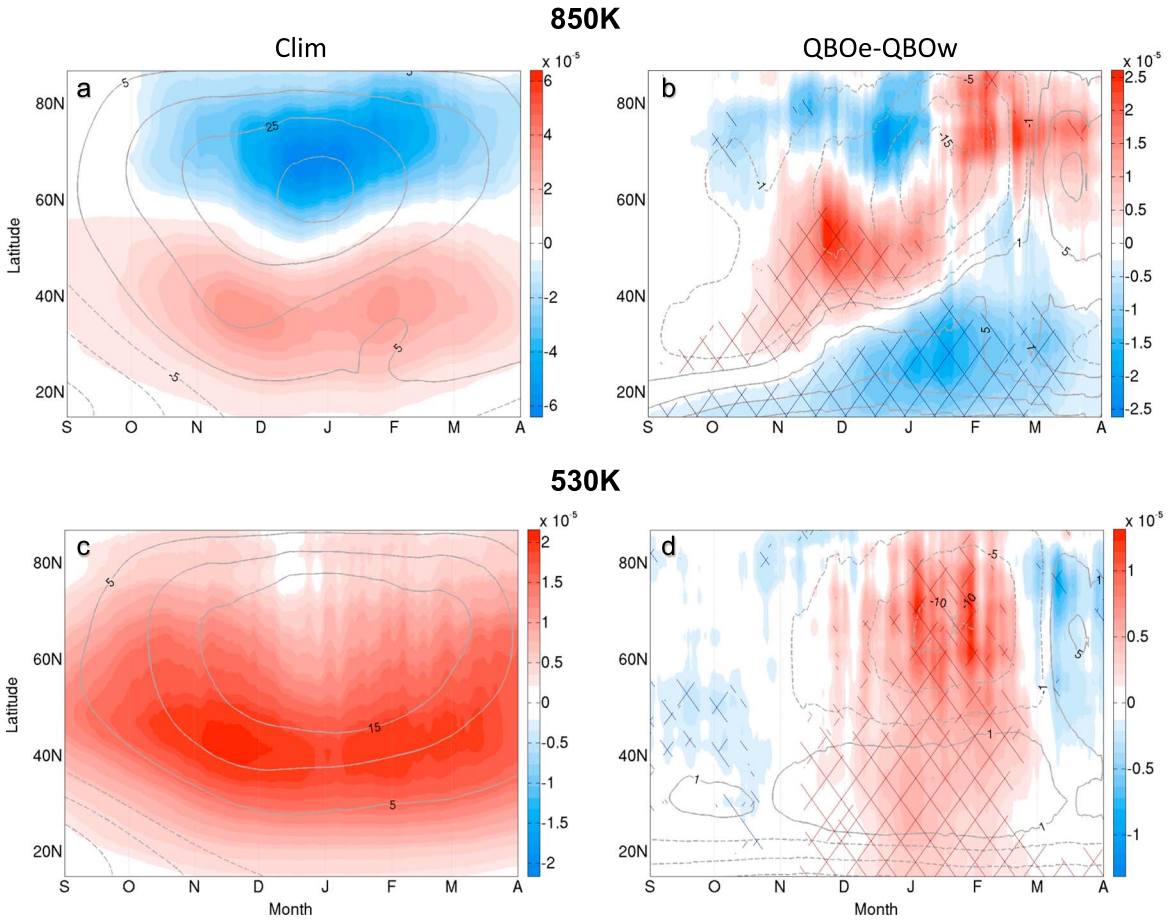


**Figure 3.** Seasonal progression of the climatology and QBO composite difference of the mean meridional circulation term Θ at 850 K (a and b) and at 530 K (c and d). The unit of Θ is m $s^{-2}$. As in Figure 2, the contours represent the corresponding zonal-wind climatologies (±5, 15, 25,… m $s^{-1}$) and QBO-induced anomalies (±1, 2, 3, … m $s^{-1}$), and the hatching indicates the statistical significance.

The QBO effect on eddy fluxes at 850 K is marked by negative $\overline{\sigma v' P'}$ anomalies (i.e., equatorward PV fluxes) poleward of ~50°N during November–February and positive anomalies (i.e., poleward PV fluxes), in the subtropics to midlatitudes under QBOe. This dipole pattern suggests a meridional redistribution of PV, which leads to positive and negative PV anomalies around a latitude circle in the intervening region, indicative of enhanced wave disturbances within the polar vortex. Furthermore, this dipole pattern of $\overline{\sigma v' P'}$ anomalies appear to migrate poleward over winter, dynamically consistent with the poleward migration of the zonal-wind anomalies in the same region (contours). At 530 K, the anomalies throughout the subtropics to high latitudes are negative in November–February, indicating enhanced wave convergence throughout the lower stratosphere. These negative anomalous PV fluxes are in agreement with the isentropic-coordinate EP flux convergence anomalies found in this region associated with the fountain-like wave-propagating feature by *White et al.* [2015] in the December–February mean. The positive anomalous PV fluxes at 530 K found in March are indicative of a change in wave forcing due to the early winter onset of the weaker polar vortex at this level.

In addition to causing mean flow changes, the stratospheric wave forcing shown in Figure 2 is closely related to the meridional circulation. Here we analyze the QBO modulation of the horizontal advection of absolute vorticity $\Theta = -\hat{v}\left((\overline{u}\cos\varphi)_{\varphi}/a\cos\varphi - f\right)$ (equation (2)). Note that the vertical-advection term is not included in Θ (see equation (1)); thus, Θ does not account for the full circulation associated with the Brewer-Dobson circulation. Figures 3a and 3c show the seasonal evolution of the climatological Θ at 850 K and 530 K respectively, with positive (negative) Θ representing a poleward (equatorward) advection. At 850 K, the climatology of Θ is marked by a dipole pattern, with a poleward advection in the subtropics to midlatitudes and an

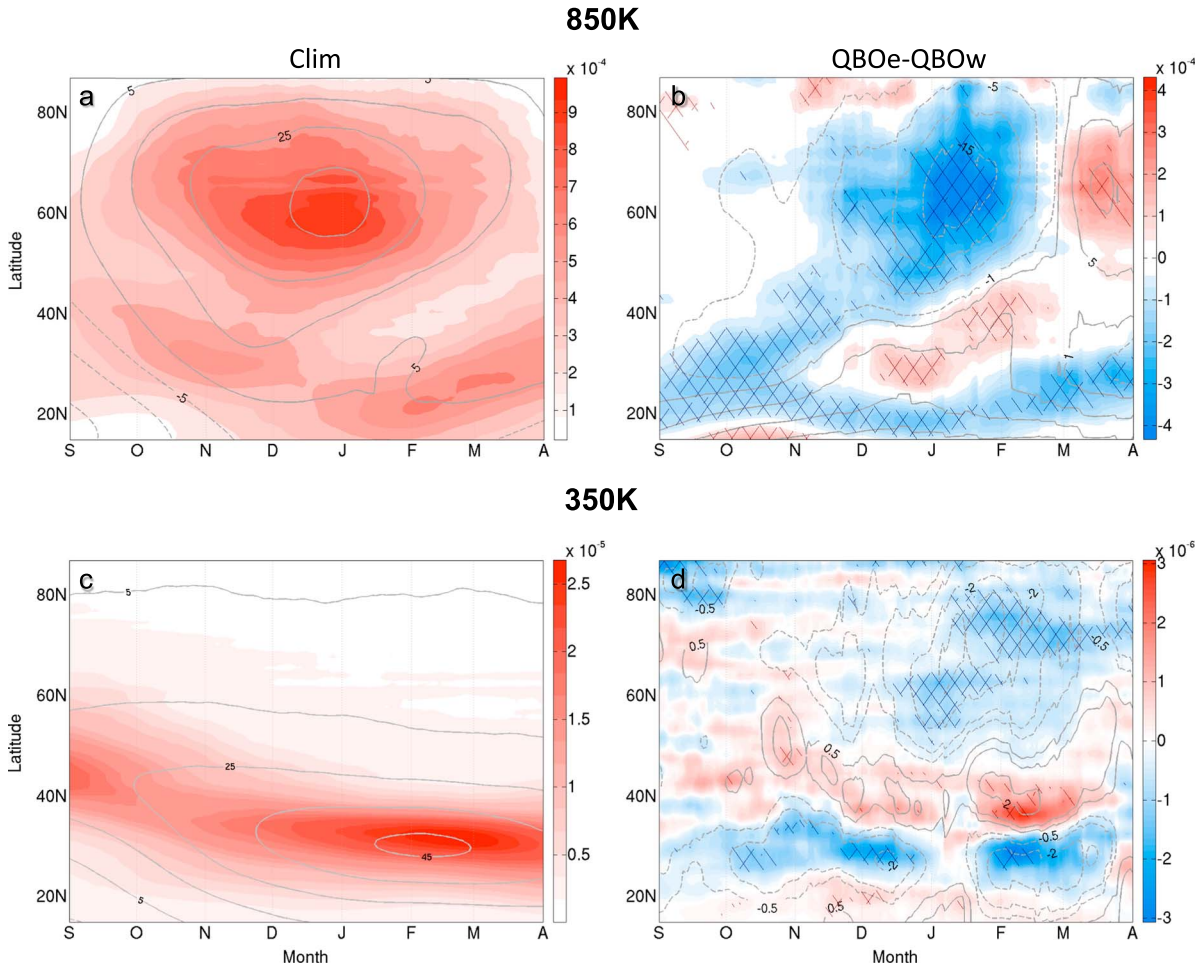


**Figure 4.** Seasonal progression of the climatology and QBO composite difference of the meridional PV gradient $\overline{P}_{\varphi}$ at 850 K (a and b) and at 350 K (c and d). $\overline{P}_{\varphi}$ has units of K m$^2$ kg$^{-1}$ s$^{-1}$ per degree. Same as in Figure 2, the contours represent corresponding zonal wind climatologies or QBO-induced anomalies, while the hatching indicates the statistical significance.

equatorward advection at high latitudes. The equatorward advection at high latitudes is associated with the zonal-mean meridional velocity $\overline{v}$ (not shown). This is consistent with the findings of *Hitchman and Huesmann* [2009], who found a similar $\overline{v}$ feature on isentropic levels ranging from ~800 K to 1700 K. At 530 K, the climatological Θ is predominately positive throughout the extratropics with a noticeable peak at midlatitudes, indicative of an overall poleward advection.

Figures 3b and 3d show the QBO-induced Θ anomalies at 850 K and 530 K. At 850 K, the Θ anomalies tend to closely follow the poleward progression of the zonal-wind anomalies (contours), with the positive Θ anomalies migrating poleward from the subtropics to midlatitudes during early to midwinter. The negative Θ anomalies that initiated near the tropics also migrate poleward to ~40°N during middle to late winter. These low-latitude anomalies agree with the poleward shift of the QBO-induced meridional circulation [*Jones et al.*, 1998; *Lu et al.*, 2014]. The poleward migration of these dipole-patterned Θ anomalies also correspond well to the wave-forcing anomalies (Figure 2b). At 530 K, there is no sign of a poleward migration of the Θ anomalies. Instead, from mid-November to late February, there is an overall strengthened poleward advection throughout the extratropics. As the midlatitude Θ anomalies are positive at both levels, they indicate an overall enhanced poleward advection under QBOe.

Figure 4 shows the seasonal evolution of the climatology of the meridional PV gradient $\overline{P}_{\varphi}$ at 850 K (a) and at 350 K (c), with the corresponding QBO-induced anomalies shown in Figures 4b and 4d, respectively. Note that $\overline{P}_{\varphi}$ provides some of the key information on the ability of Rossby-wave propagation, with $\overline{P}_{\varphi} > 0$ permitting

propagation and $\overline{P}_\varphi < 0$ prohibiting propagation [*Charney and Drazin,* 1961] (also, see *White et al.* [2015] for a full discussion on the relation between $\overline{P}_\varphi$ and the waveguide). In terms of the climatology, $\overline{P}_\varphi > 0$ dominates the extratropical stratosphere and troposphere during the extended boreal winter. Largest $\overline{P}_\varphi$ values are found near the edge of the polar vortex at ~60°N, 850 K and near the subtropical jet core at ~30°N, 350 K.

The QBO signature in $\overline{P}_\varphi$ at 850 K is predominantly marked by the negative $\overline{P}_\varphi$ anomalies that migrate poleward from the subtropics to high latitudes during October–February under QBOe. This poleward migration is in agreement with the other diagnostics presented in Figures 1b, 2b, and 3b. Further, the negative $\overline{P}_\varphi$ anomalies in the subtropics at 850 K, which occur throughout the winter period, are an expected feature on the flank of the QBO westerlies at this level. This is due to the fact that there are strong QBO westerlies equatorward of weak subtropical westerlies, which help to form a sharp westerly QBO jet profile in the tropics [e.g., *Shuckburgh et al*., 2001]. We also note that positive $\overline{P}_\varphi$ anomalies have migrated poleward from 30°N during middle to late winter, exactly following the shear zone of the zonal-wind anomalies (contours).

At 350 K, the $\overline{P}_\varphi$ QBO anomalies exhibit two key features: the first is the region of poleward migrating negative $\overline{P}_\varphi$ anomalies at high latitudes, corresponding to the negative $\overline{P}_\varphi$ anomalies at 850 K. A seasonal delay is evident at 350 K when compared to those at 850 K, which is associated with the downward descent of the HTE over winter (see Figure 1c). Also, the negative $\overline{P}_\varphi$ anomalies at high latitudes in middle to late winter are associated with the negative polar-vortex anomalies of the HTE. The second key feature is the dipole of positive and negative anomalies on the poleward and equatorward flanks of the subtropical jet, respectively. They are associated with the poleward shift of the subtropical jet and indicate a poleward shift of the waveguide in the midlatitude lower stratosphere throughout the winter. These waveguide anomalies become increasingly significant at levels up to 530 K (not shown) and appear to be intensified during late winter.

To examine the effect of the QBO-induced change of the waveguide on wave propagation in the middle stratosphere, the horizontal component of the EP flux $F^{(\varphi)} = -a\bar{\sigma}\cos\varphi\overline{v'u'}$ at 850 K is analyzed. Note that $F^{(\varphi)} < 0$ indicates equatorward wave propagation, and $F^{(\varphi)} > 0$ indicates poleward propagation. $F^{(\varphi)}$, with contributions from the total wave fluxes, planetary waves (zonal wave numbers 1 and 2) and synoptic waves (zonal wave numbers 3–10) are shown, respectively, in Figures 5a, 5c, and 5e. We note that these results are not sensitive to our definition of synoptic waves as qualitatively similar results can be obtained if synoptic waves are defined as waves with zonal wave numbers of 5–10 instead. In the climatology of total wave fluxes (Figure 5a), $F^{(\varphi)}$ is predominately equatorward throughout the winter, with largest-magnitude equatorward fluxes at ~50–60°N and during November–February as the waves are refracted by the strong westerlies near the edge of the polar vortex. Figure 5c suggests that these fluxes are dominated by planetary waves, whereas the contribution from synoptic waves is noticeably smaller (Figure 5e). Also note that the region of most negative synoptic wave $F^{(\varphi)}$ is located farther equatorward than that of the planetary waves.

The prominent feature of the QBO-induced changes in meridional propagation of the total wave fluxes (Figure 5b) is the region of anomalous poleward wave propagation throughout the subtropics to midlatitudes under QBOe. These anomalies in poleward wave propagation extend to high latitudes in January–March with noticeably enhanced strength and with magnitudes comparable to its climatological values. The poleward $F^{(\varphi)}$ anomalies also follow the boundary between the positive and negative $\overline{P}_\varphi$ anomalies (Figure 4b), indicating a change in horizontal wave propagation associated with a poleward refraction of the waves due to the negative $\overline{P}_\varphi$ anomalies. From Figure 5d it can be seen that planetary waves largely account for the anomalous poleward-propagating waves in late winter. In early winter, however, the planetary waves only exhibit equatorward $F^{(\varphi)}$ anomalies at low latitudes which are not in dynamical agreement with the HTE. The QBO-induced synoptic-wave anomalies are marked by a band of poleward migrating positive $F^{(\varphi)}$ anomalies in the subtropics to midlatitudes which occur throughout the extended winter period and start in September–October (Figure 5f). Note that these anomalies are an order of magnitude smaller than the planetary-wave anomalies. This feature broadly follows the waveguide shown by the $\overline{P}_\varphi$ anomalies (Figure 4b).

The height-time evolution of $F^{(\varphi)}$ is shown in Figure 6 with the climatology in contours and the composite difference in shading. In Figures 6a and 6c, $F^{(\varphi)}$ is averaged over 30–40°N and is split into wave contributions from the total and planetary 1–2. Figures 6b and 6d show the same as 6a and 6c except for $F^{(\varphi)}$ averaged over

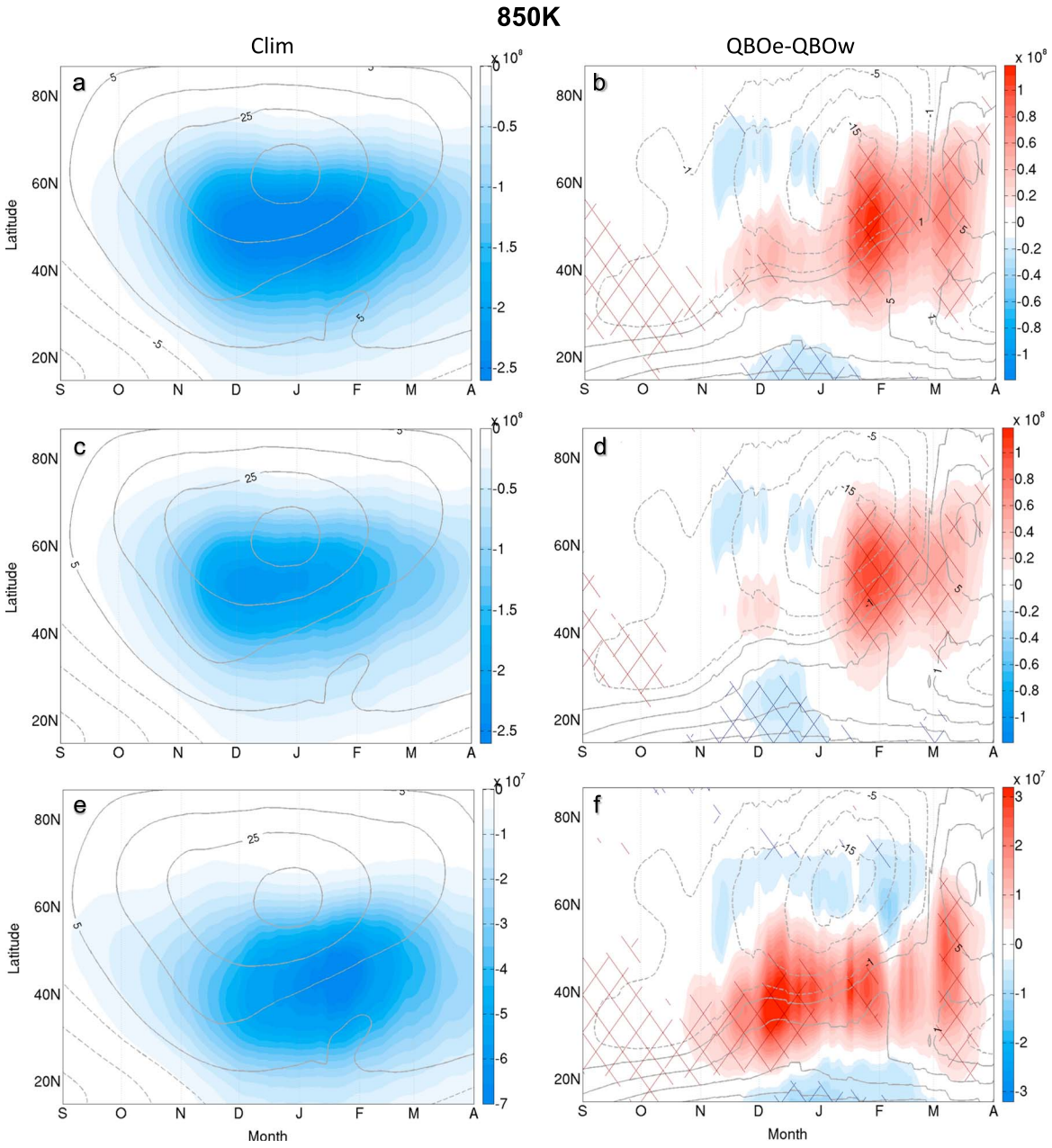


**Figure 5.** Seasonal progression of the climatology and QBO composite difference of the horizontal component of the EP flux $F^{(\varphi)}$ at 850 K, where (a and b) are the total $F^{(\varphi)}$, (c and d) the planetary wave (i.e., waves 1 and 2) contribution, and (e and f) the synoptic wave (i.e., waves 3–10) contribution. The units of $F^{(\varphi)}$ are in kg m $K^{-1}$ $s^{-2}$. Same as in Figure 2, the contours represent corresponding zonal wind climatology or QBO-induced anomalies, while the hatching indicates statistical significance. Note the difference in magnitudes of the colorbars between the total- and planetary-wave panels and the synoptic-wave panel.

60–70°N. These two latitude bands are chosen to best coincide with the equatorward and poleward branches of the anomalous EP flux fountain-like feature found by *White et al.* [2015, Figure 6]. The $F^{(\varphi)}$ climatology at 30–40°N is everywhere negative indicating equatorward wave propagation, with the largest-magnitude $F^{(\varphi)}$ near the tropopause. In the stratosphere, the largest-magnitude values of $F^{(\varphi)}$ are found during December–February. Planetary waves mostly account for the stratospheric $F^{(\varphi)}$ and also some toward the $F^{(\varphi)}$ near the tropopause. In the composite difference at 30–40°N, the total $F^{(\varphi)}$ (Figure 6a) shows negative anomalies from early November to March, indicating anomalous equatorward wave propagation toward the zero-wind line in the lower stratosphere. There are also small-valued positive anomalies, indicating poleward wave propagation above 600 K. Planetary waves account for the early to midwinter lower

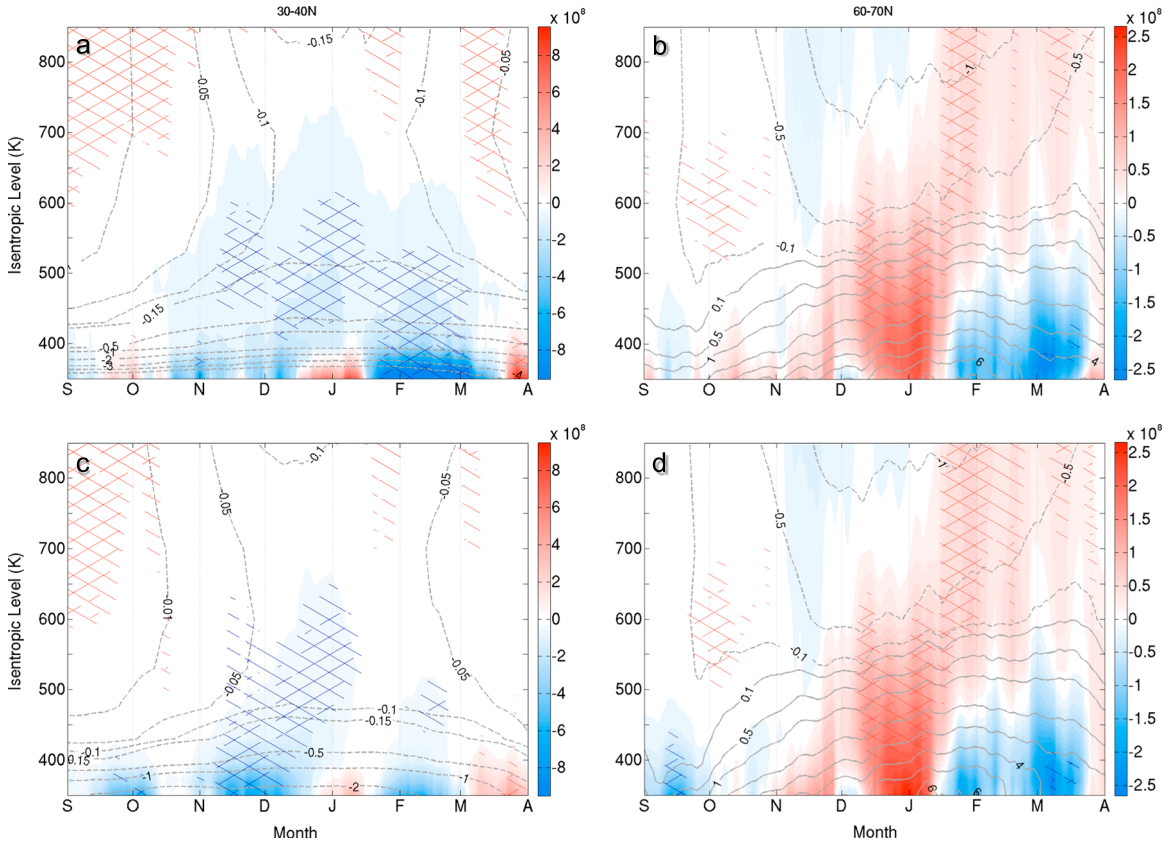


**Figure 6.** (a and c) Seasonal progression of the climatology (contours) and composite difference (shading) of $F^{(\varphi)}$ averaged over 30–40°N in a time-height cross section for total-wave (Figure 6a) and planetary-wave 1 and 2 (Figure 6c) contributions. Positive values indicate poleward wave propagation, whereas negative values indicate equatorward propagation. Climatological contours are at −0.01, −0.05, −0.1, −0.15, −0.5, −1, −2, −3,…×$10^9$ kg m $K^{-1}$ $s^{-2}$. (b and d) Same as Figures 6a and 6c except averaged over the latitude band of 60–70°N for the total (Figure 6b) and planetary-wave 1 and 2 (Figure 6d) contributions, and with climatological contours at ±0.1, 0.5, 1, 2, 3,…×$10^8$ kg m $K^{-1}$ $s^{-2}$. Hatching as in Figure 1.

stratospheric anomalies (Figure 6c), whereas we note that synoptic waves contribute toward the late winter anomalies (not shown).

At 60–70°N, the climatological total $F^{(\varphi)}$ (Figure 6b) shows a vertical dipole pattern, with equatorward wave propagation in the middle stratosphere, likely due to refraction by the strong polar vortex, and smaller-magnitude poleward wave propagation in the lower stratosphere. This dipole persists throughout the winter, attaining largest magnitudes during November–February. It appears that planetary waves fully account for the climatological $F^{(\varphi)}$, with synoptic waves only playing a minor role near the tropopause at this latitude band (not shown). The composite difference is mainly marked by positive anomalies, indicating enhanced poleward wave propagation under QBOe, in dynamical agreement with the HTE. These high-latitude anomalies in the lower stratosphere are dominated by planetary waves (Figure 6d) and appear to occur approximately 1 month later than the equatorward anomalies at 30–40°N (Figures 6a and 6c). This suggests that these midwinter high-latitude planetary-wave anomalies may be induced by the enhanced wave breaking near the subtropical zero-wind line and consequent poleward wave refraction/reflection in early winter [*Tung,* 1979]. In the middle stratosphere, the signal is mainly found in late winter, with enhanced anomalous poleward wave propagation that is again accounted for by planetary waves. This feature is in agreement with Figure 5d. The region of positive anomalies in October at 500–700 K is relatively small valued, occurring prior to the onset of the HTE and hence likely plays a minimal role. We note that there is no significant contribution from synoptic waves in this latitude band (not shown).

To examine the changes of wave activity near the zero-wind line, the enstrophy budget (equation (3)) at 530 K for the November–January average is shown in Figure 7, for the latitude range of 10–50°N. Figure 7a shows the climatology of each of the individual terms that contribute to the enstrophy tendency ($\partial\left(\overline{P'^2}/2\right)/\partial t$).

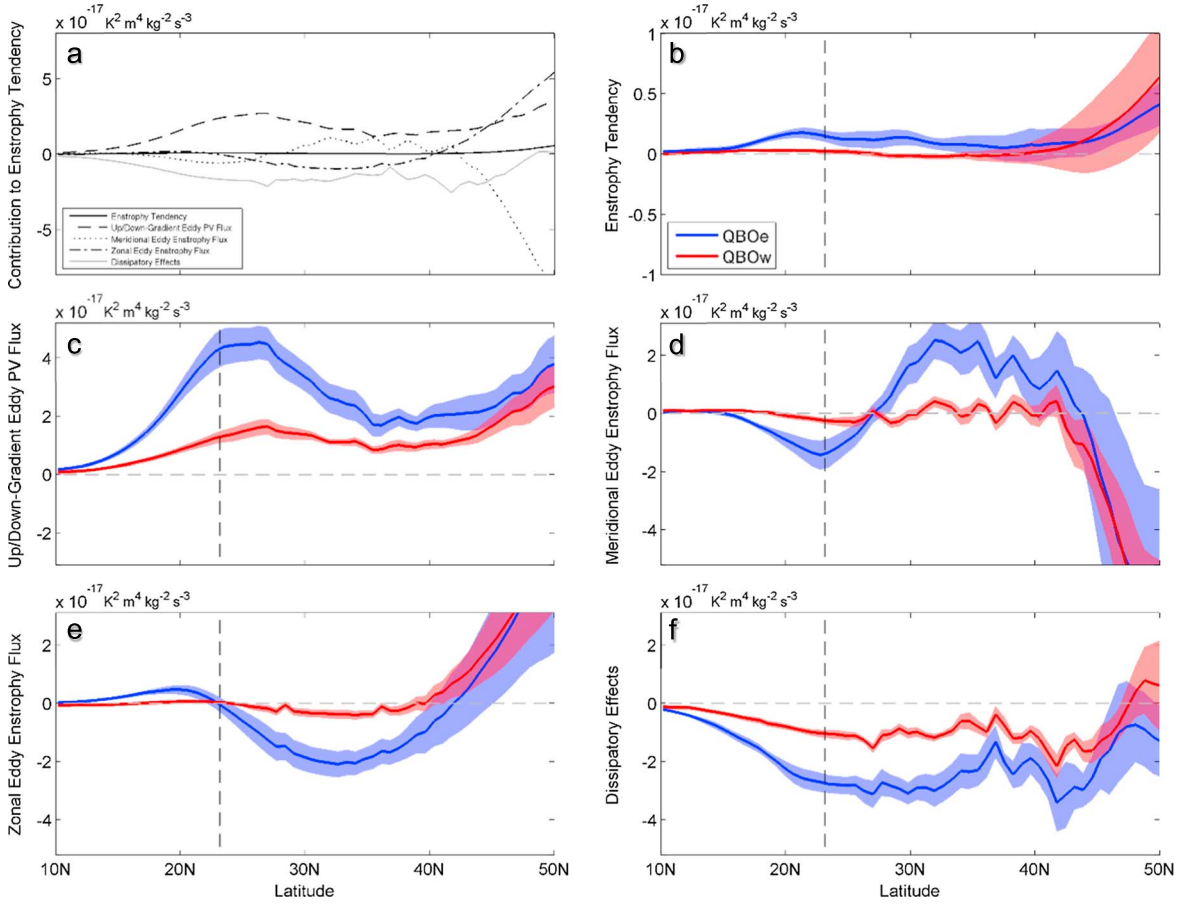


**Figure 7.** (a) November–January climatology of each of the terms in the enstrophy balance (equation (3)) at 530 K, over the latitude band of 10–50°N. Each term is presented as a contribution to the enstrophy tendency $\partial\left(\overline{P'^2}/2\right)/\partial t$ (solid black line), with the dashed, dotted, dash-dotted, and solid grey lines representing the up/downgradient eddy PV flux term $\Gamma_{WMI}$, meridional eddy enstrophy flux term $\Gamma_{MEEF}$, zonal eddy enstrophy flux term $\Gamma_{ZEEF}$, and dissipatory effects $D_2$ calculated as the residual of the other terms, respectively. Note that positive values indicate positive enstrophy tendencies (i.e., local wave growth) and vice versa. Units in $K^2\,m^4\,kg^{-2}\,s^{-3}$. (b–f) November–January average of each of the terms $\partial\left(\overline{P'^2}/2\right)/\partial t$, $\Gamma_{WMI}$, $\Gamma_{MEEF}$, $\Gamma_{ZEEF}$, and $D_2$, respectively, under QBOe (blue) and QBOw (red) conditions. As in Figure 7a, each term is calculated as its contribution to $\partial\left(\overline{P'^2}/2\right)/\partial t$. Shaded regions indicate the 95% confidence intervals under each QBO phase, colored accordingly. Vertical black dashed line indicates the location of the zero-wind line under QBOe. Grey horizontal dashed line indicates a value of $\partial\left(\overline{P'^2}/2\right)/\partial t = 0$ for reference. Units as in Figure 7a.

Although of small magnitude, the enstrophy tendencies are generally positive and increase with latitude. These small enstrophy tendencies result from a cancelation between the noticeably larger terms on the right-hand side of equation (3). In particular, downgradient eddy PV fluxes ($\Gamma_{WMI} > 0$) contribute positive enstrophy tendencies which increase wave amplitudes, while dissipatory effects ($D_2$) act to induce negative enstrophy tendencies and hence reduce wave amplitudes. In terms of the nonlinear terms, the zonal and meridional eddy enstrophy fluxes ($\Gamma_{ZEEF}$ and $\Gamma_{MEEF}$) tend to balance each other, with approximately equal and opposite contributions to the overall enstrophy tendency.

Figures 7b–7f show the individual terms in the enstrophy budget under QBOe and QBOw. It is evident that the magnitude and the variability associated with each term is generally larger under QBOe than QBOw. More specifically, there is significantly enhanced positive enstrophy tendencies throughout 15–35°N (Figure 7b) under QBOe, indicating an overall larger wave activity in this region. Increased downgradient eddy PV fluxes ($\Gamma_{WMI} > 0$) (Figure 7c) and enhanced negative dissipatory effects ($D_2 < 0$) (Figure 7f) are found throughout 10–45°N under QBOe. Increased divergence of meridional eddy enstrophy fluxes ($\Gamma_{MEEF} < 0$) is found near the QBOe zero-wind line (15–25°N) (Figure 7d) along with convergent zonal eddy enstrophy fluxes ($\Gamma_{ZEEF} > 0$) (Figure 7e). The net effect of these nonlinear terms is a divergence of eddy enstrophy fluxes away from the zero-wind line. Enhanced convergence of meridional eddy enstrophy

fluxes ($\Gamma_{MEEF} > 0$) is indeed found farther northward at 30–40°N, which is approximately balanced by increased divergent zonal eddy enstrophy fluxes ($\Gamma_{ZEEF} < 0$). This indicates a nonlinear enstrophy transfer between the zonal and meridional directions under QBOe. Note that the nonlinear terms are an order of magnitude smaller under QBOw at these latitudes, suggesting that the climatological values of these terms (Figure 7a) are dominated by QBOe. Thus, nonlinear wave-wave interactions in the lower stratosphere are significantly enhanced under QBOe and the effect extends from the zero-wind line to midlatitudes.

To understand how changes in the waveguide in the stratosphere can modulate the upward propagation of wave activity from the troposphere and to determine if the anomalous horizontal-propagating waves at 850 K and in the lower stratosphere can be attributed to changes in wave activity below, the vertical component of the EP flux $F^{(\theta)}$ at 350 K is examined in Figure 8. The 350 K level is chosen to represent wave propagation from the troposphere to the stratosphere as it represents one of the "middle-world" isentropic levels that crosses the tropopause (near 30°N) but does not reach down to the surface [e.g., *Hoskins,* 1991]. Qualitatively similar results are found on surrounding isentropic surfaces ranging from 300 K to 395 K (not shown), corresponding to the lower levels of the fountain-like feature in the EP fluxes shown by *White et al.* [2015]. The seasonal evolution of the climatology of $F^{(\theta)}$ and their associated QBO composite differences is separately presented for the total, stationary planetary, transient planetary, and synoptic-wave contributions, which we hereafter refer to as total $F^{(\theta)}$, stationary $F^{(\theta)}$, transient planetary $F^{(\theta)}$, and synoptic $F^{(\theta)}$ for brevity. The most prominent feature of the climatological total $F^{(\theta)}$ (Figure 8a) is the upward propagation of wave activity (indicated by positive $F^{(\theta)}$), which extends from ~30°N on the poleward flank of the subtropical jet to ~60°N and persists throughout the winter period, peaking during November–February. Both the climatological stationary planetary waves (Figure 8c) and synoptic waves (Figure 8g) account for the total upward propagation of wave activity with ~50% each, while the transient planetary-wave contribution (Figure 8e) is approximately an order of magnitude smaller in terms of the climatology. On the equatorward flank of the subtropical jet, however, there are negative values of $F^{(\theta)}$, indicative of downward wave propagation. We note that these negative values at 10–25°N are located in the troposphere at this level and so are subject to influences such as the change in lapse rate across the tropopause. Because there is no QBO signal in this region (see Figures 8b, 8d, and 8f) and because it would digress from the main aims of this paper, we shall ignore this subtropical region of climatological negative $F^{(\theta)}$ hereafter.

Figure 8b suggests that there is an overall anomalous increase in the total upward propagation of wave activity at midlatitudes throughout the winter period under QBOe, extending farther poleward in early winter than in late winter. The stationary $F^{(\theta)}$ (Figure 8d) exhibits three centers of enhanced anomalous upward-propagating wave activity, at 30–40°N in October–December, 50–65°N in November–January, and poleward of 65°N in January–February. These anomalies indicate a poleward migration of the wave activity over winter and are dynamically agreeable to the HTE. The QBO-induced changes in transient planetary $F^{(\theta)}$ (Figure 8f) are marked by the negative anomalies at high latitudes during January–February with magnitudes comparable to its climatology, indicative of less upward transient planetary-wave propagation inside the polar vortex under QBOe. This is agreeable to the change in high-latitude waveguide associated with the wind structure of the HTE itself (Figure 4d). It is worth noting that unlike the climatology, the magnitude of these transient planetary $F^{(\theta)}$ anomalies is comparable to the stationary $F^{(\theta)}$ anomalies indicating that the QBO has a significant effect on transient planetary waves at high latitudes after the onset of the HTE. The difference plot of synoptic $F^{(\theta)}$ suggests that enhanced upward synoptic-wave propagation under QBOe is in close proximity to the poleward shifted subtropical jet and the corresponding poleward shift of the waveguide in the region, with the largest upward anomalies occurring in late winter. We note that these synoptic-wave anomalies are contributed to mostly by zonal wave numbers 3 and 4 (not shown). Overall, these QBO-induced $F^{(\theta)}$ anomalies indicate that there is a clear seasonal progression of the different wave types, and each may play different roles in early and late winter.

Figure 9 allows us to examine the vertical extent of the upward-propagating wave-activity anomalies by showing the vertical seasonal evolution of the stationary $F^{(\theta)}$, transient planetary $F^{(\theta)}$, and synoptic $F^{(\theta)}$ over the latitude bands where the strongest QBO signatures are found in Figure 8. Figure 9a shows the climatology (contours) and QBO-induced anomalies (shading) of the stationary $F^{(\theta)}$ averaged over the latitude band of 50–60°N in a time-height cross section. In the climatology, the stationary $F^{(\theta)}$ is upward throughout 350–850 K during the extended winter period, but with a distinct seasonal cycle; it penetrates weakly into

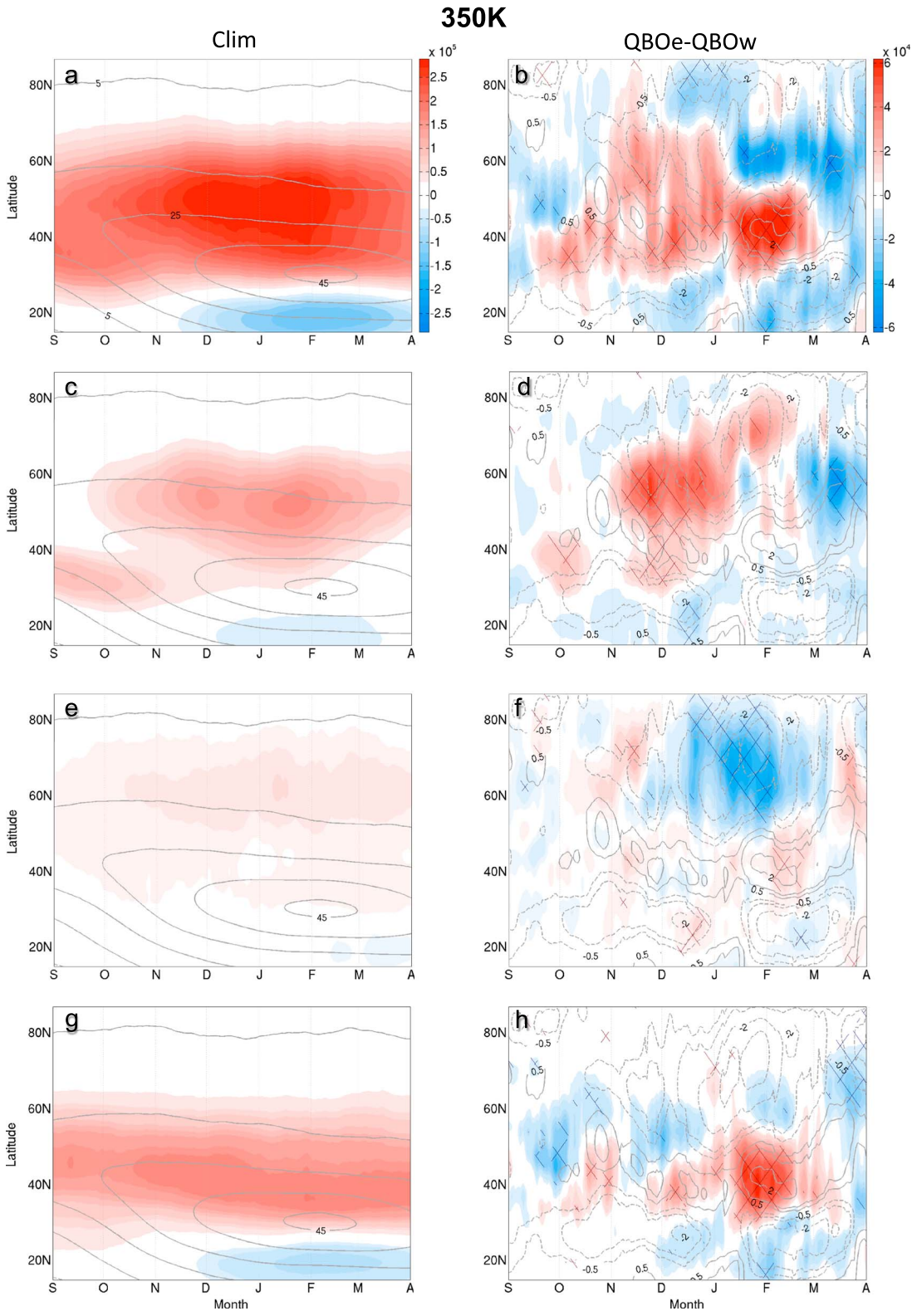


**Figure 8.** Seasonal progression of the climatology and QBO composite difference of the vertical component of the EP flux $F^{(\theta)}$ at 350 K, where (a and b) are the total $F^{(\theta)}$, (c and d) the stationary planetary-wave contribution, (e and f) the transient planetary-wave contribution, and (g and h) is the synoptic-wave contribution. The contours represent corresponding zonal-wind climatology or QBO-induced anomalies, while the hatchings indicate the statistical significance, as in Figure 2. Units of $F^{(\theta)}$ are in kg $s^{-2}$. Note the difference in color scale between the climatologies in the left-hand panels and the composite difference in the right-hand panels. The climatologies are approximately 5 times larger than the composite differences.

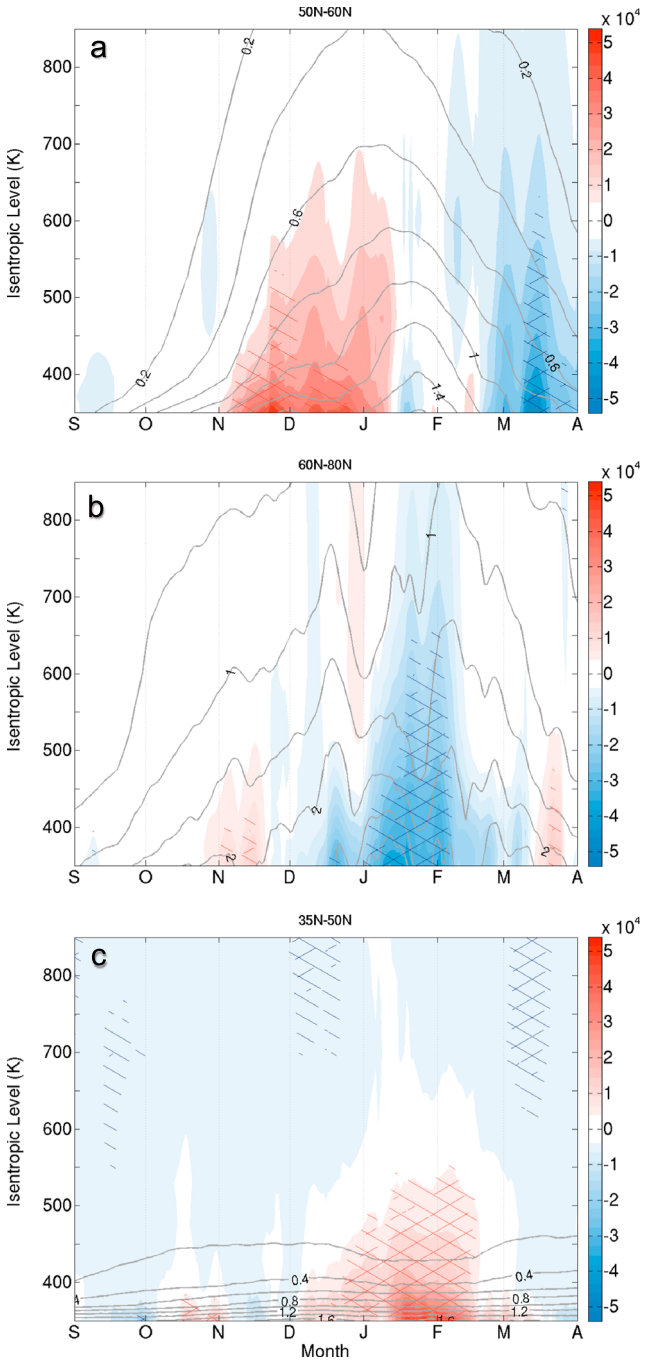


**Figure 9.** (a) Seasonal progression of the climatology (contours) and composite difference (shading) of the stationary planetary-wave contribution to $F^{(\theta)}$ averaged over the latitude band of 50–60°N in a time-height cross section. Positive values indicate upward fluxes of wave activity, whereas negative values indicate downward fluxes. Contours in the climatology have an interval of $0.2 \times 10^5$ kg s$^{-2}$. (b) Same as Figure 9a except for the transient planetary-wave contribution to $F^{(\theta)}$ averaged over 60–80°N with a climatological contour interval of $0.5 \times 10^4$ kg s$^{-2}$. (c) Same as Figure 9a except for the synoptic-wave contribution to $F^{(\theta)}$ averaged over 35–50°N. Note the difference in climatological contour interval between Figures 9a and 9c and 9b.

the stratosphere in September–October, before reaching higher isentropic levels during November–February and finally starting to be capped again in the upper troposphere-lower stratosphere from March. This is consistent with the classic theory for upward-propagating planetary waves [*Charney and Drazin*, 1961], whereby, for instance, it can be estimated that for stationary planetary-wave 1, the threshold wind speed for wave propagation at 60°N is ~28 m s$^{-1}$ (compare with Figure 1c) [*Andrews et al.*, 1987]. In the composite difference, the predominant feature is the positive $F^{(\theta)}$ anomalies during November–December, indicative of enhanced upward-propagating stationary-wave activity. These positive anomalies penetrate up to ~530 K in late November, becoming much weaker above this level.. This is suggestive of the upward propagation of wave activity being modulated in some way in the lower stratosphere, most likely by the changes in the wind structure and circulation. We also note the negative anomalies in March, which are dynamically consistent with the positive wind anomalies in the same period.

Figure 9b shows the vertical seasonal evolution of the climatology (contours) and composite difference (shading) of the transient planetary $F^{(\theta)}$ averaged over 60–80°N. Note that the climatological transient planetary $F^{(\theta)}$ is an order of magnitude smaller than that of the stationary $F^{(\theta)}$, as in Figure 8e. Nevertheless, it exhibits a similar seasonal cycle to the stationary $F^{(\theta)}$ with the waves penetrating deepest into the stratosphere during November–February. The QBO-induced anomalous transient planetary $F^{(\theta)}$ is characterized by the small and relatively brief positive anomalies in early winter, which extend into the lowermost stratosphere (~400 K). During January–February, there are negative anomalies that extend from the troposphere to the middle stratosphere. While the early winter positive anomalies may contribute toward the initial onset of the HTE, the late winter

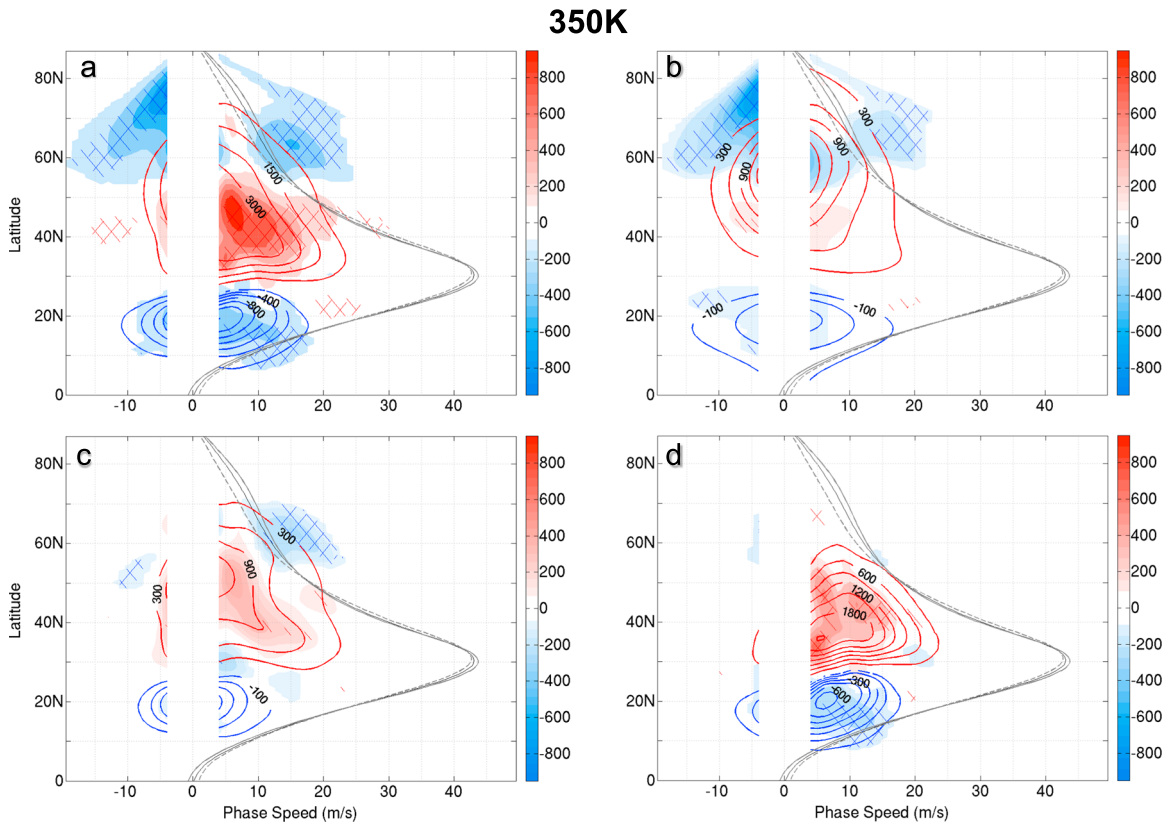


**Figure 10.** (a) Latitude-phase-speed cospectra of the DJFM climatology (red and blue contours) and QBO composite difference (shading) of the vertical component of the EP flux $F^{(\theta)}$ at 350 K for zonal wave-numbers 1–10. Climatological red contours are at 750, 1500, 2250,… kg s$^{-2}$, and blue contours are at −200, −400, −600,… kg s$^{-2}$. Cospectra for phase speeds $|c| \leq 4$ m s$^{-1}$ are not plotted because such phase speeds cannot be resolved reliably by this analysis. (b–d) Same as Figure 10a except for zonal-wave numbers 1 and 2 (i.e., planetary wave), zonal-wave numbers 3 and 4 (i.e., intermediate wave), and zonal-wave numbers 5–10 (i.e., synoptic wave) contributions to Figure 10a. Cimatological contours in Figures 10b–10d have an interval of 300, 600, 900,… kg s$^{-2}$ and −100, −200, −300,… kg s$^{-2}$, respectively. The thick black line indicates the climatological zonal-mean zonal wind $\bar{u}$, whereas the thin and dashed black lines indicate $\bar{u}$ averaged over the QBOw and QBOe DJFM periods, respectively. Hatchings are as in Figure 1.

negative anomalies indicate that less transient planetary waves are able to enter the stratosphere at high latitudes due to the seasonal change in the wind structure associated with the HTE.

The climatology (contours) and composite difference (shading) of the synoptic $F^{(\theta)}$ averaged over 35–50°N in the time-height cross section is shown in Figure 9c. In the climatology, the synoptic $F^{(\theta)}$ is capped mostly within the troposphere, which is perhaps expected according to the theory of *Charney and Drazin* [1961]. In the composite difference however, positive synoptic $F^{(\theta)}$ anomalies extend from 350 K to ~530 K in late winter with values that are comparable to its climatology in the stratosphere, suggesting that more synoptic waves are able to propagate into the stratosphere if the background state is changed favorably under QBOe. As such, the effect is enhanced after the onset of the HTE.

To better understand the later-winter transient-wave response to the HTE, we further elucidate on the QBO modulation of the upward propagation of these waves across the tropopause by analyzing phase-speed spectra of $F^{(\theta)}$ at 350 K over December to March (DJFM) (Figure 10). It shows the climatology (red and blue contours) and composite difference (shading) of the latitude-phase-speed cospectrum, summed over zonal wave-numbers 1–10 (Figure 10a), 1 and 2 (Figure 10b), 3 and 4 (Figure 10c), and 5 and 10 (Figure 10d). In the climatologies, the key features are the dipole patterns centered on the subtropical jet core near 30° N, with upward wave propagation at ~30–70°N and downward wave propagation at ~10–25°N (see Figure 8). It shows that eastward-propagating waves dominate the climatological synoptic wave (waves 5–10) and intermediate-wave (waves 3 and 4) cospectra, with the largest-magnitude cospectra having phase speeds of $c \approx 10$–$15$ m s$^{-1}$. In the planetary-wave (waves 1 and 2) cospectrum, however, the largest-magnitude cospectrum values occur at phase speeds smaller than the minimum resolved phase

speed of ~4 m s$^{-1}$. This is suggestive of quasi-stationary ($c \approx 0$ m s$^{-1}$) planetary waves being a large contributor to the total upward planetary-wave cospectrum. Also, note that the peaks in the $F^{(\theta)}$ cospectra of waves 1 and 2 and waves 3 and 4 are located farther poleward than that of the waves 5–10. This is in qualitative agreement with Figure 8, indicating that low wave-number waves are more likely to propagate into the stratosphere at high latitudes than high wave-number waves. Overall, the cospectra for all wave-number bands appear to be broadly confined to eastward phase speeds smaller than the critical phase speed $\bar{u} = c$, as predicted by linear theory.

In the extratropics, the QBO modulation of the upward-propagating transient wave activity across the tropopause is identified primarily at two distinct latitude bands: reduced upward transient wave propagation (i.e., negative anomalies) at high latitudes associated with both westward and eastward-propagating waves and enhanced upward wave propagation (i.e., positive anomalies) at midlatitudes which is largely associated with synoptic-scale eastward-propagating waves. At high latitudes, the negative westward anomalies with phase speeds of $c = -4$ to $-10$ m s$^{-1}$ are accounted for mainly by waves 1 and 2, implying that planetary waves are responsible for those changes. This is in agreement with the negative transient planetary-wave anomalies at high latitudes seen in Figures 8f and 9b. Further, the negative cospectrum anomalies associated with both westward ($c = -10$ to $-20$ m s$^{-1}$) and eastward ($c = 10$–$20$ m s$^{-1}$) phase speeds near 60–70°N have comparable magnitudes, indicating a decrease in standing planetary waves at those latitudes. In addition, waves 3 and 4 contribute to the negative eastward anomalies at 60–70°N. Note that these negative eastward anomalies occur at faster phase speeds than the critical line $\bar{u} = c$, suggesting a possible breakdown of the linear theory and a transition into a nonlinear wave regime. Overall, these cospectra anomalies suggest that under QBOe, there is an increase in upward eastward-propagating synoptic waves at midlatitudes and a reduction in westward-propagating and standing planetary waves at high latitudes during DJFM, which occur as a consequence to the circulation and waveguide changes associated with the early to midwinter HTE.

## 4. Summary and Discussion

The seasonal evolution of the Holton-Tan effect (HTE) and its mechanisms have been studied via examining changes in the extratropical circulation and wave forcing during the extended Northern Hemisphere winter (September–March). This has been accomplished using the ERA-Interim reanalysis data set and a range of wave-mean-flow interaction and wave-wave interaction diagnostics in isentropic coordinates. It shows that quasi-stationary planetary waves, transient planetary waves, and synoptic waves all play a role at different stages throughout the winter. In particular, stationary planetary waves play a role in early winter, whereas transient planetary waves and synoptic waves are modulated in late winter due to the early winter onset of the HTE. Both linear and nonlinear wave interactions have also been found to play a role in the QBO modulation of wave activity in the lower stratosphere under QBOe.

Our results indicate that in the lower stratosphere, early winter (October–December) is characterized by increased upward stationary planetary-wave propagation from the troposphere into the stratosphere under QBOe. Transient planetary waves also play a minor role, whereas synoptic waves do not appear to contribute to the onset of the HTE in the lower stratosphere. This enhanced upward flux appears to be due to a combination of two mechanisms: (1) the QBO's influence on the zero-wind line in the lower stratosphere which encourages more upward stationary planetary-wave propagation [*Holton and Tan,* 1980] and (2) the QBO-induced meridional circulation induces downward-arching baroclinic zonal-wind anomalies in the subtropics midlatitudes, which lead to a poleward shift of the subtropical jet and corresponding waveguide, and thus encourages more upward wave propagation across the tropopause "valve" [*Chen and Robinson,* 1992]. It is nevertheless difficult to quantify the relative contributions of each of these two mechanisms for causing enhanced upward wave propagation across the tropopause solely from reanalysis data and also given the fact that the poleward shift of the waveguide near the subtropical jet is stronger in late winter than in early winter.

The enhanced upward-propagating waves into the lower stratosphere form a fountain-like feature in the Eliassen-Palm (EP) fluxes, whereby there are equatorward-propagating waves toward the zero-wind line and poleward-propagating waves toward the polar vortex, as shown in *White et al.* [2015]. Here it is found that this fountain-like feature evolves throughout the winter, with equatorward-propagating wave anomalies in November and poleward-propagating wave anomalies occurring approximately 1 month later.

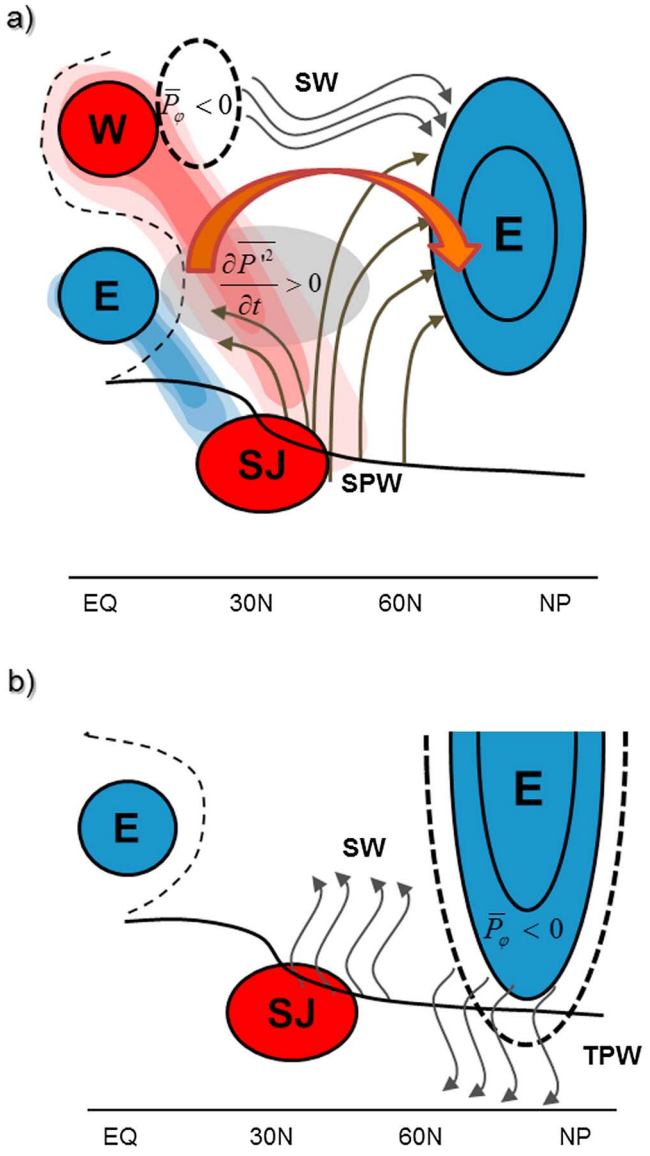


**Figure 11.** (a) Schematic diagram showing the early winter HTE. The equatorial vertical wind dipole pattern with the blue (E; easterly) and red (W; westerly) anomalies represents the QBO winds, and the thin dashed black line is the QBO-induced critical line. The blue oval at high latitudes represents the weakened polar vortex under QBOe (i.e., the HTE), and the red oval near the tropopause (i.e., thick black line) at 30°N represents the approximate location of the subtropical jet (SJ). The vertically-sheared red and blue shaded regions that arch down from the QBO winds to near the tropopause represent the downward arching zonal winds associated with the QBO-induced meridional circulation. The grey shaded region represents anomalous wave growth (i.e., wave breaking) ($\partial \overline{P'^2}/\partial t > 0$). The grey arrows indicate the approximate direction of anomalous synoptic wave (SW) and anomalous stationary planetary wave propagation, whereas the thick orange arrow from the subtropics to high latitudes represents the enhanced wave-driven meridional circulation under QBOe. The heavy dashed black oval at 20–30°N represents the negative PV gradient anomalies which act to reflect SW's poleward. (b) Schematic diagram of the late winter HTE. Anomalous reduced upward travelling planetary waves can be seen at high latitudes. See text for further details.

The enstrophy budget analysis suggests that both linear and nonlinear effects contribute to this enhanced meridional propagation of wave activity under QBOe, with the nonlinear effects being much reduced under QBOw. The zero-wind line under QBOe appears to act as an absorber of wave activity, indicated by increased downgradient eddy PV fluxes (approximately EP flux convergence) [*Haynes,* 1989]. There is also evidence of possible nonlinear wave reflection under QBOe, with enhanced divergent meridional eddy enstrophy fluxes near the zero-wind line. The net effect of the nonlinear eddy enstrophy fluxes near the zero-wind line is to apply negative enstrophy tendencies and hence reduce the enstrophy locally, in agreement with *Robinson* [1988]. These meridional eddy enstrophy fluxes converge at midlatitudes and induce further nonlinear wave-wave interactions in this region. This is seemingly in agreement with the lifecycle of a critical layer where wave activity is first absorbed and then reflected and over-reflected, becoming a perfect reflector in the long-time limit [*Killworth and McIntyre,* 1985]. The enhanced wave breaking associated with the fountain-like feature under QBOe, as evidenced by enhanced enstrophy growth throughout the subtropics to midlatitudes, is consistent with a stronger meridional circulation in the lower stratosphere, which aids in the high-latitude warming and weaker polar vortex. The fountain-like feature and the associated wave growth/breaking is shown schematically in Figure 11a.

In the middle stratosphere, early winter is instead characterized by predominately poleward wave propagation (Figure 11a). More specifically, waves that propagate into the middle stratosphere are refracted poleward by the subtropical negative PV gradient induced by the presence of the strong equatorial QBO westerlies [*Shuckburgh et al.*, 2001] near 700–850 K. These waves consequently converge at high latitudes and thus weaken the polar vortex. A feedback

process appears to cause an overall poleward migration of the upper level anomalies during the winter, whereby the refracted waves break at middle to high latitudes, driving a stronger poleward meridional circulation, which in turn "drags" poleward the subtropical negative PV gradient and induces latitudinal shifts in the regions of wave propagation and breaking. These results in the middle stratosphere are in agreement with the mechanism proposed by *Garfinkel et al.* [2012] and *Lu et al.* [2014]. Additionally, our results further indicate that the poleward-propagating waves are dominated by synoptic waves in October–January with planetary waves only becoming important during January–March. These synoptic waves may be generated in situ in the QBO westerlies in the middle stratosphere as found by *Shuckburgh et al.* [2001]. Overall, the enhanced wave breaking in the lower and middle stratosphere acts to strengthen the meridional circulation which aids in the adiabatic warming at high latitudes and concurrently the weaker polar vortex associated with the HTE.

The early winter onset of the HTE in turn affects the high-latitude waveguide and hence the late winter (January–March) upward propagation of wave activity from the troposphere. This is because the polar-vortex anomalies associated with the HTE descend down to the tropopause region in midwinter, which consequently affects the high-latitude waveguide (Figure 11b). Under QBOe, this manifests as a decrease in upward transient and standing planetary waves at high latitudes and an increase in upward synoptic waves at midlatitudes. This feature is in agreement with the modeling experiments of *Lachmy and Harnik* [2014], who found that a poleward shift of the subtropical jet causes a decrease in westward-propagating planetary waves at high latitudes and an increase in synoptic waves at midlatitudes. These results can therefore be used to explain the aforementioned findings of previous authors that showed variations in wave-1 and wave-2 anomalies during the winter season calculated using only seasonal averages [e.g., *Holton and Tan,* 1982; *Hu and Tung,* 2002; *Naito and Yoden,* 2006; *Naoe and Shibata*, 2010].

It is understood that the QBO has the potential to provide improved predictability of the surface weather at seasonal to interannual timescales [*Boer and Hamilton*, 2008; *Marshall and Scaife*, 2009; *Smith et al.*, 2012]. It also plays a crucial role in other teleconnections, including the joint effect of the 11 year solar cycle and the QBO on the polar vortex [e.g., *Labitzke and van Loon*, 1988; *Lu et al.*, 2009]. Understanding the pathways by which the QBO affects the extratropical circulations, therefore, is a key step toward explaining other related changes in both the stratosphere and the troposphere. This study has contributed toward this goal through a comprehensive examination of the seasonal evolution of the HTE and its associated changes in wave activity using a range of isentropic diagnostics. Further work is needed to ensure the validity of these findings, especially with the use of controlled model experiments, which would allow a better examination of the causal links between the different mechanisms. Additionally, this study only used isentropic data extending into the middle stratosphere (850 K). To better understand the influence of the QBO on the extratropical circulation throughout the depth of the stratosphere, future studies must include isentropic data in the upper stratosphere.

**Acknowledgments**
This study is funded by the Natural Environment Research Council (NERC). I.W. is funded by NERC PhD studentship NE/K50094X/1. We acknowledge use of ECMWF ERA-Interim data sets (http://apps.ecmwf.int/datasets/data/interim-full-daily). We thank the constructive suggestions from Gang Chen regarding the cospectrum analysis. We also wish to thank the constructive comments from the reviewers which have greatly improved the clarity of the manuscript.

## References

Andrews, D. G. (1987), On the interpretation of the Eliassen-Palm flux divergence, *Q. J. R. Meteorol. Soc.*, *113*, 323–338.
Andrews, D. G., J. R. Holton, and C. B. Leovy (1987), Middle Atmosphere Dynamics, *Int. Geophys. Ser.*, vol. 40, 489 pp., Academic Press, New York.
Anstey, J. A., T. G. Sheperd, and J. F. Scinocca (2010), Influence of the quasi-biennial oscillation on the extratropical winter stratosphere in an atmospheric general circulation model and in reanalysis data, *J. Atmos. Sci.*, *67*, 1402–1419.
Baldwin, M. P., et al. (2001), The quasi-biennial oscillation, *Rev. Geophys.*, *39*(2), 179–229, doi:10.1029/1999RG000073.
Birner, T., D. W. J. Thompson, and T. G. Shepherd (2013), Up-gradient eddy fluxes of potential vorticity near the subtropical jet, *Geophys. Res. Lett.*, *40*, 5988–5993, doi:10.1002/2013GL057728.
Boer, G., and K. Hamilton (2008), QBO influence on extratropical predictive skill, *Clim. Dyn.*, *31*, 987–1000.
Butler, A. H., D. W. J. Thompson, and T. Birner (2011), Isentropic slopes, downgradient eddy fluxes, and the extratropical atmospheric circulation response to tropical tropospheric heating, *J. Atmos. Sci.*, *68*, 2292–2305.
Calvo, N., M. A. Giorgetta, R. Garcia-Herrera, and E. Manzini (2009), Nonlinearity of the combined warm ENSO and QBO effects on the Northern Hemisphere polar vortex in MAECHAM5 simulations, *J. Geophys. Res.*, *114*, D13109, doi:10.1029/2008JD011445.
Charney, J. G., and P. G. Drazin (1961), Propagation of planetary scale disturbances from the lower into the upper atmosphere, *J. Geophys. Res.*, *66*(1), 83–109, doi:10.1029/JZ066i001p00083.
Chen, P., and W. A. Robinson (1992), Propagation of planetary waves between the troposphere and stratosphere, *J. Atmos. Sci.*, *49*, 2533–2545.
Dee, D. P., et al. (2011), The ERA-Interim reanalysis: Configuration and performance of the data assimilation system, *Q. J. R. Meteorol. Soc.*, *137*(656), 553–597.
Edmon, H. J., B. J. Hoskins, and M. E. McIntyre (1980), Eliassen-Palm cross sections for the troposphere, *J. Atmos. Sci.*, *37*, 2600–2616.
Garfinkel, C. I., and D. L. Hartmann (2011), The influence of the quasi-biennial oscillation on the troposphere in winter in a hierarchy of models. Part I: Simplified dry GCMs, *J. Atmos. Sci.*, *68*, 1273–1289.
Garfinkel, C. I., T. A. Shaw, D. L. Hartmann, and D. W. Waugh (2012), Does the Holton-Tan mechanism explain how the quasi-biennial oscillation modulates the Arctic polar vortex?, *J. Atmos. Sci.*, *69*, 1713–1733.

Gray, L. J., S. J. Phipps, T. J. Dunkerton, M. P. Baldwin, E. F. Drysdale, and M. R. Allen (2001), A data study of the equatorial upper stratosphere on Northern Hemisphere stratospheric sudden warmings, *Q. J. R. Meteorol. Soc.*, *127*(576), 1985–2003.

Gray, L. J., S. Crooks, C. Pascoe, S. Sparrow, and M. Palmer (2004), Solar and QBO influences on the timing of stratospheric sudden warmings, *J. Atmos. Sci.*, *61*, 2777–2796.

Haynes, P. H. (1989), The effect of barotropic instability on the nonlinear evolution of a Rossby-wave critical layer, *J. Fluid Mech.*, *207*, 231–266.

Haynes, P. H., and M. E. McIntyre (1987), On the evolution of vorticity and potential vorticity in the presence of diabatic heating and frictional and other forces, *J. Atmos. Sci.*, *44*, 828–841.

Hitchman, M. H., and A. S. Huesmann (2009), Seasonal influence of the quasi-biennial oscillation on stratospheric jets and Rossby wave breaking, *J. Atmos. Sci.*, *66*, 935–946.

Holton, J. R., and H. C. Tan (1980), The influence of the equatorial quasi-biennial oscillation on the global circulation at 50 mb, *J. Atmos. Sci.*, *37*, 2200–2208.

Holton, J. R., and H. C. Tan (1982), The quasi-biennial oscillation in the Northern Hemisphere lower stratosphere, *J. Meteorol. Soc. Jpn.*, *60*, 140–148.

Hoskins, B. J. (1991), Towards a PV-θ view of the general circulation, *Tellus*, *43AB*, 27–35.

Hoskins, B. J., M. E. McIntyre, and W. A. Robertson (1985), On the use and significance of isentropic potential vorticity maps, *Q. J. R. Meteorol. Soc.*, *111*, 877–946.

Hu, Y., and K. K. Tung (2002), Tropospheric and equatorial influences on planetary-wave amplitude in the stratosphere, *Geophys. Res. Lett.*, *29*(2), 1019, doi:10.1029/2001GL013762.

Jones, D. B. A., H. R. Schneider, and M. B. McElroy (1998), Effects of the quasi-biennial oscillation on the zonally averaged transport of tracers, *J. Geophys. Res.*, *103*(D10), 11,235–11,249, doi:10.1029/98JD00682.

Killworth, P. D., and M. E. McIntyre (1985), Do Rossby-wave critical layers absorb, reflect or over-reflect?, *J. Fluid Mech.*, *161*, 449–492.

Kunz, T., K. Fraedrich, and F. Lunkeit (2009), Impact of synoptic-scale wave breaking on the NAO and its connection with the stratosphere in ERA-40, *J. Clim.*, *22*, 5464–5480.

Labitzke, K., and H. van Loon (1988), Association between the 11-year solar cycle, the QBO and the atmosphere. Part I: The troposphere and stratosphere in the Northern Hemisphere in winter, *J. Atmos. Sol. Terr. Phys.*, *50*(3), 197–206.

Lachmy, O., and N. Harnik (2014), The transition to a subtropical jet regime and its maintenance, *J. Atmos. Sci.*, *71*, 1389–1409.

Lu, H., M. P. Baldwin, L. J. Gray, and M. J. Jarvis (2008), Decadal-scale changes in the effect of the QBO on the Northern stratospheric polar vortex, *J. Geophys. Res.*, *113*, D101114, doi:10.1029/2007JD009647.

Lu, H., L. J. Gray, M. P. Baldwin, and M. J. Jarvis (2009), Life cycle of the QBO-modulated 11-year solar cycle signals in the Northern Hemispheric winter, *Q. J. R. Meteorol. Soc.*, *135*, 1030–1043.

Lu, H., D. Pancheva, P. Mukhtarov, and I. Cnossen (2012), QBO modulation of travelling planetary waves during northern winter, *J. Geophys. Res.*, *117*, D09104, doi:10.1029/2011JD016901.

Lu, H., T. J. Bracegirdle, T. Phillips, A. Bushell, and L. J. Gray (2014), Mechanisms for the Holton-Tan relationship and its decadal variation, *J. Geophys. Res. Atmos.*, *119*, 2811–2830, doi:10.1002/2013JD021352.

Madden, R. A., and K. Labitzke (1981), A free Rossby wave in the troposphere and stratosphere during January 1979, *J. Geophys. Res.*, *86*(C2), 1247–1254, doi:10.1029/JC086iC02p01247.

Marshall, A. G., and A. A. Scaife (2009), Impact of the QBO on surface winter climate, *J. Geophys. Res.*, *114*, D18110, doi:10.1029/2009JD011737.

Martius, O., C. Schwarz, and H. C. Davies (2007), Breaking waves at the tropopause in the wintertime Northern Hemsiphere: Climatological analyses of the orientation and the theoretical LC1/2 classification, *J. Atmos. Sci.*, *64*, 2576–2592.

McIntyre, M. E., and T. N. Palmer (1983), Breaking planetary waves in the stratosphere, *Nature*, *305*, 593-600.

Naito, Y., and S. Yoden (2006), Behavior of planetary waves before and after stratospheric sudden warming events in several phases of the equatorial QBO, *J. Atmos. Sci.*, *63*, 1637–1649.

Naoe, H., and K. Shibata (2010), Equatorial quasi-biennial oscillation influence on Northern Hemisphere winter extratropical circulation, *J. Geophys. Res.*, *115*, D19102, doi:10.1029/2009JD012952.

Newman, P. A., E. R. Nash, and J. E. Rosenfield (2001), What controls the temperature of the Arctic stratosphere during the spring?, *J. Geophys. Res.*, *106*, 19,999–20,010, doi:10.1029/2000JD000061.

O'Sullivan, D., and R. E. Young (1992), Modeling the quasi-biennial oscillation's effect on the winter stratospheric circulation, *J. Atmos. Sci.*, *49*, 2437–2448.

O'Sullivan, D., and T. J. Dunkerton (1994), Seasonal development of the extratropical QBO in a numerical model of the middle atmosphere, *J. Atmos. Sci.*, *51*, 3706–3721.

Pascoe, C. L., L. J. Gray, and A. A. Scaife (2006), A GCM on the study of the influence of equatorial winds on the timing of stratospheric sudden warmings, *Geophys. Res. Lett.*, *33*, L06825, doi:10.1029/2005GL024715.

Plumb, R. A., and R. C. Bell (1982), A model of the quasi-biennial oscillation on an equatorial beta-plane, *Quart. J. Roy. Meteorol. Soc.*, *108*, 335–352, doi:10.1002/qj.49710845604.

Randel, W. J., and I. M. Held (1991), Phase speed spectra of transient eddy fluxes and critical layer absorption, *J. Atmos. Sci.*, *48*(5), 688–697.

Robinson, W. A. (1988), Irreversible wave–mean flow interactions in a mechanistic model of the stratosphere, *J. Atmos. Sci.*, *45*, 3413–3430.

Ruzmaikin, A., J. Feynman, X. Jiang, and Y. L. Yung (2005), Extratropical signature of the quasi-biennial oscillation, *J. Geophys. Res.*, *110*, D11111, doi:10.1029/2004JD005382.

Shuckburgh, E. F., W. A. Norton, A. Iwi, and P. H. Haynes (2001), The influence of the quasi-biennial oscillation on isentropic transport and mixing in the tropics and subtropics, *J. Geophys. Res.*, *106*(D13), 14,327–14,338, doi:10.1029/2000JD900664.

Smith, A. K. (1983), Observation of wave-wave interactions in the stratosphere, *J. Atmos. Sci.*, *40*, 2484–2496.

Smith, A. K. (1985), Wave transience and wave-mean flow interaction caused by the interference of stationary and traveling waves, *J. Atmos. Sci.*, *42*, 529–535.

Smith, D., A. A. Scaife, and B. Kirtman (2012), What is the current state of scientific knowledge with regard to seasonal and decadal forecasting?, *Environ. Res. Lett.*, *7*, 015602.

Tung, K. K. (1979), A theory of stationary long waves. Part III: Quasi-normal modes in a singular waveguide, *Mon. Weather Rev.*, *107*, 751–774.

Watson, P. A. G., and L. J. Gray (2014), How does the quasi-biennial oscillation affect the stratospheric polar vortex?, *J. Atmos. Sci.*, *71*, 391–409.

White, I. P., H. Lu, N. J. Mitchell, and T. Phillips (2015), Dynamical response to the QBO in the northern winter stratosphere: Signatures in wave forcing and eddy fluxes of potential vorticity, *J. Atmos. Sci.*, *72*, 4487–4507.

Yamashita, Y., H. Akiyoshi, and M. Takahashi (2011), Dynamical response in the Northern Hemisphere midlatitude and high-latitude winter to the QBO simulated by CCSR/NIES CCM, *J. Geophys. Res.*, *116*, D06118, doi:10.1029/2010JD015016.